Direct and semidirect aerosol effects of southern African biomass burning aerosol

Naoko Sakaeda,[1] Robert Wood,[1] and Philip J. Rasch[2]

Received 21 December 2010; revised 15 March 2011; accepted 24 March 2011; published 21 June 2011.

[1] Direct and semidirect radiative effects of biomass burning aerosols from southern African fires during July–October are investigated using 20 year runs of the Community Atmospheric Model (CAM) coupled to a slab ocean model. Aerosol optical depth is constrained using observations in clear skies from Moderate Resolution Imaging Spectroradiometer (MODIS) and for aerosol layers above clouds from Cloud Aerosol Lidar and Infrared Pathfinder Satellite Observation (CALIPSO). Over the ocean, where the aerosol layers are primarily located above cloud, negative top of atmosphere (TOA) semidirect radiative effects associated with increased low cloud cover dominate over a weaker positive all-sky direct radiative effect (DRE). In contrast, over the land where the aerosols are often below or within cloud layers, reductions in cloud liquid water path (LWP) lead to a positive semidirect radiative effect that dominates over a near-zero DRE. Over the ocean, the cloud response can be understood as a response to increased lower tropospheric stability (LTS) which is caused both by radiative heating in overlying layers and surface cooling in response to direct aerosol forcing. The marine cloud changes are robust to changes in the cloud parameterization (removal of the hard-wired dependence of clouds on LTS), suggesting that they are physically realistic. Over land, decreased LWP is consistent with weaker convection driven by increased static stability. Over the entire region the overall TOA radiative effect from the biomass burning aerosols is almost zero due to opposing effects over the land and ocean. However, the surface forcing is strongly negative, which leads to a reduction in precipitation and also a reduction in sensible heat flux. The former is primarily realized through reductions in convective precipitation on both the southern and northern flanks of the convective precipitation region spanning the equatorial rain forest and the Intertropical Convergence Zone (ITCZ) in the southern Sahel. The changes are consistent with the low-level aerosol-forced cooling pattern. The results highlight the importance of semidirect radiative effects and precipitation responses for determining the climatic effects of aerosols in the African region.

Citation: Sakaeda, N., R. Wood, and P. J. Rasch (2011), Direct and semidirect aerosol effects of southern African biomass burning aerosol, *J. Geophys. Res.*, *116*, D12205, doi:10.1029/2010JD015540.

1. Introduction

[2] The effects of aerosols emitted by biomass burning on Earth's radiation budget are significant but their magnitude and extent are not yet fully understood [*Schulz et al.*, 2006; *Ramanathan and Carmichael*, 2008]. Southern Africa is a region characterized by intense biomass burning emissions during the months of June to October [*Cooke et al.*, 1996]. Biomass burning contributes to over 86% of the total global emissions of black carbon soot, and the largest source of biomass burning emissions is the African savannas [*Levine et al.*, 1995]. These emissions form extensive aerosol layers which advect primarily westward over the southeastern Atlantic Ocean [e.g., *Matichuk et al.*, 2007; *Chand et al.*, 2009], where they overlay vast decks of stratocumulus clouds.

[3] The reflection and absorption of solar radiation by aerosols changes the radiative balance of the lower atmosphere and may plausibly induce feedbacks on clouds and the hydrological cycle [e.g., *Lau et al.*, 2006]. Climate model studies have found that the climate sensitivity to absorbing aerosols such as black carbon can be two or more times larger than the sensitivity to carbon dioxide for a given top-of-atmosphere (TOA) radiative forcing [*Hansen et al.*, 1997; *Cook and Highwood*, 2004]. This is in part because, in addition to the aerosol direct effect, models show a reduction in cloudiness driven by the aerosol heating profile [*Ackerman et al.*, 2000], a response termed the semidirect aerosol effect [*Hansen et al.*, 1997]. Studies have also indicated that there may be important aerosol indirect effects

[1]Department of Atmospheric Sciences, University of Washington, Seattle, Washington, USA.
[2]Pacific Northwest National Laboratory, Richland, Washington, USA.

0148-0227/11/2010JD015540

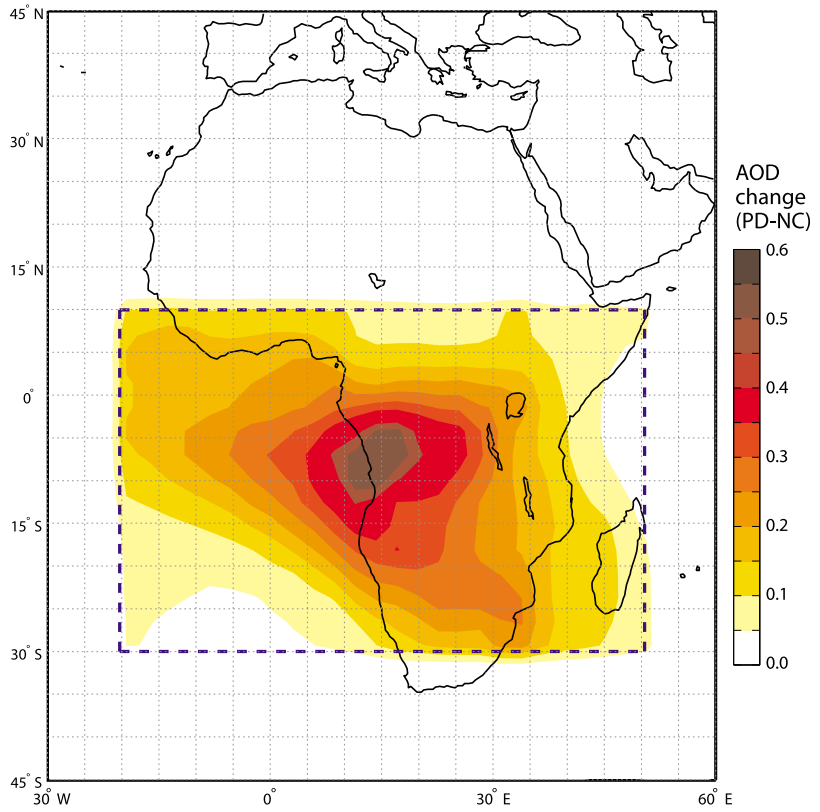

Figure 1. Change in AOD between simulation with and without carbonaceous. The dashed box represents the region where carbonaceous aerosol mass is modified.

associated with absorbing aerosols acting as cloud condensation nuclei that may partially cancel their warming effect [*Chen et al.*, 2010].

[4] Observations indicate that, for a given aerosol single scattering albedo, the direct radiative forcing efficiency (direct radiative forcing per unit of aerosol optical depth) depends primarily on the amount of cloud cover [*Chand et al.*, 2009] since it is dependent on the albedo of the underlying surface, be this a cloud or the Earth's surface [*Chýlek and Coakley*, 1974]. Over the southeastern Atlantic, there is no consensus in the models as to the sign or magnitude of the direct aerosol forcing [*Schulz et al.*, 2006], and this may be caused in part by differences in the representation of clouds across models. Observationally derived estimates, assuming plausible single scattering albedos, indicate that the aerosol TOA direct forcing over the southeastern Atlantic switches from positive to negative for regions where the cloud cover exceeds about 40% [*Keil and Haywood*, 2003; *Abel et al.*, 2005; *Chand et al.*, 2009].

[5] The semidirect aerosol effect is caused by a change in cloud cover or cloud liquid water path due to heating from aerosol absorption of solar radiation. *Morgan et al.* [2006] found a lack of consensus as to the sign and magnitude of the global semidirect effect among 24 expert atmospheric and climate scientists, while estimates of direct and indirect effects were more consistent among the experts. Unraveling the uncertainties in the semidirect effects is important as some studies found that the magnitude of semidirect effects could exceed the direct forcing [*Johnson et al.*, 2004] and the atmospheric feedback processes that arise from semidirect effects could play an important role explaining the total aerosol radiative effect [*Lau et al.*, 2010].

[6] Several studies have estimated semidirect effects on global and regional scales [*Hansen et al.*, 1997; *Penner et al.*, 2003; *Cook and Highwood*, 2004; *Johnson et al.*, 2004; *Allen and Sherwood*, 2010], but little consistency is seen among their results. *Johnson et al.* [2004] examined the dependence of the aerosol radiative effect on the vertical distribution of aerosols. They found that the sign of direct and semidirect effects can be different depending on whether absorbing aerosol is located above, in, or both in and above the boundary layer. Other studies [*Cook and Highwood*, 2004; *Yoshimori and Broccoli*, 2008; *Sud et al.*, 2009; *Allen and Sherwood*, 2010] also recognize the dependence of the vertical distribution of aerosols on the radiative forcing. It is also known that the semidirect effect estimated from modeling studies is dependent on the cloud scheme of the models [*Cook and Highwood*, 2004]. While there are several plausible hypotheses for how clouds respond to absorbing aerosols, these hypotheses have not been fully tested and numerous questions remain. For example, to what extent might reductions in downwelling solar radiation impact clouds underlying aerosol layers, compared with changes in the lower tropospheric static stability that are observed to impact cloud cover [*Klein and Hartmann*, 1993; *Wood and Bretherton*, 2006]? Can static stability metrics derived primarily from regions without aerosol layers offer useful guidance as to the response of low clouds to overlying absorbing aerosols? And do the changes in the large-scale atmospheric circulation (e.g., vertical velocity) induced

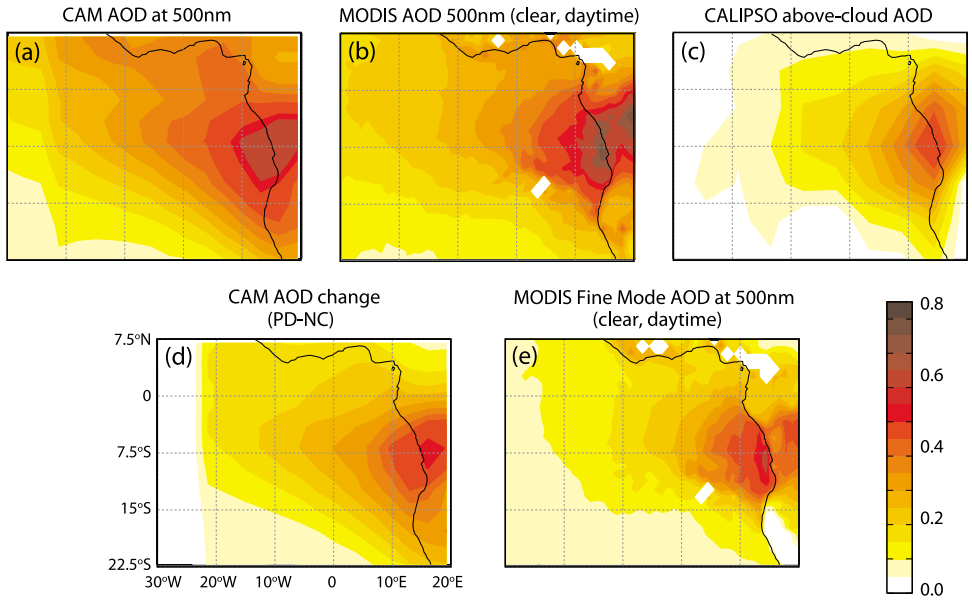

Figure 2. July–October mean AOD at 500 nm (a) for all-sky conditions from CAM (nominally at 500 nm), (b) for clear-sky conditions from MODIS, and (c) for aerosol layers above clouds from CALIPSO. (d) The difference in AOD between CAM with and without carbonaceous aerosols. (e) The MODIS fine mode fraction AOD for clear-sky conditions.

by aerosol heating also play a major role in driving cloud responses?

[7] In this study, we use a global atmospheric model coupled with a slab ocean to assess the aerosol direct and semidirect radiative effects at the regional scale associated with carbonaceous aerosols emitted by southern African biomass burning. A global model is used because regional simulations that restrict advection at the boundaries may lead to unrealistic or amplified results [*Sud et al.*, 2009]. We choose to examine a limited regional system where the configuration of aerosols and clouds is fairly simple and yet the scenarios are realistic compared with idealized models. Global studies, while all-encompassing, have the limitation of inclusion of a whole host of different aerosol-cloud configurations which renders understanding the responses more difficult. We conduct simulations with and without carbonaceous aerosols to derive the aerosol direct and semidirect effects. We break down the aerosol direct radiative effect (DRE) into that for clear sky and cloudy sky, and the semidirect effect into components caused by changes in cloud cover and liquid water path separately.

[8] Section 2 describes the numerical experiments performed, and uses observations to constrain the aerosol properties used in the model. Section 3 describes the results of the simulations, while section 4 presents a discussion and conclusions.

2. Experiments and Setup

[9] We use NCAR's global atmospheric model, the Community Atmospheric Model (CAM) Version 3.0 - Slab Ocean Model (CAM3-SOM) to interpret the impact of biomass burning aerosol layers at the regional scale. Our study focuses on the examination of direct and semidirect effect and therefore this model does not include aerosol indirect effects. The cloud nucleating properties of biomass burning aerosols may be important [*Chen et al.*, 2010], but we do not consider these effects here since CAM Version 3.0 does not resolve aerosol activation. In addition, over the ocean observations show that many of the aerosol layers are not in direct contact with the underlying cloud layers [*Costantino and Bréon*, 2010] which would imply weaker indirect effects than one might observe elsewhere. Whether the aerosol layers make contact with the cloud layers in the model is beyond the scope of this study, but is certainly worthy of additional work with a model that includes microphysical aerosol-cloud interaction.

[10] Aerosol fields are provided to the model rather than emissions, and are derived using the method by *Collins et al.* [2001] and *Rasch et al.* [2001] which uses the Model for Atmospheric Chemistry and Transport (MATCH) [*Rasch et al.*, 1997] a chemical transport model to produce model fields that are then adjusted to give approximate agreement with satellite observations (see section 2.1). The model aerosol species are natural and anthropogenic sulfate, sea salt, organic and black carbon, and dust. The aerosols are annually cyclic monthly values. Additional details are provided in the CAM Science Description document [*Collins et al.*, 2004].

[11] Two 20 year simulations are performed: one (termed PD) with present-day aerosol fields and another (termed NC) in which all the carbonaceous aerosols (organic and black carbon) are removed over the region 10°N–30°S, and 20°W–50°E (see map, Figure 1) during the main southern African biomass burning season (July–October). Most of our analysis will focus on the direct and semidirect radiative effects of the carbonaceous aerosols alone, but our comparisons with observations will necessarily include all aerosol types. During the other months when the effect of biomass burning from southern Africa is minimal, the aerosols in the two simulations are set to present-day levels.

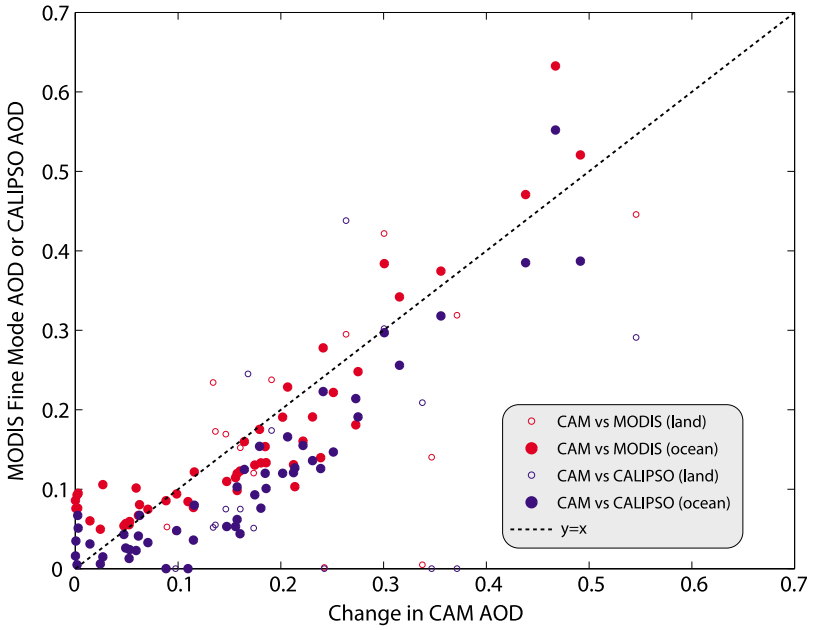

Figure 3. Observed mean aerosol optical depth (ordinate, red circles for MODIS fine-mode AOD, and blue circles for CALIPSO above-cloud AOD) plotted as a function of the mean AOD used in CAM due to carbonaceous aerosols only. Each point represents a mean over a 5 × 5° region. Solid circles indicate locations over ocean, and open circles locations over land. The dashed line shows the one-to-one line.

The carbonaceous aerosol fields in the present-day simulation are taken from the MATCH model and we found that while the geographic distribution of the aerosol optical depth matched satellite observations well, better quantitative agreement was obtained by doubling the organic and black carbon masses over the region 10°N–30°S, and 20°W–50°E. Comparisons of the model and satellite-derived aerosol fields are discussed in the next section.

2.1. Constraining the Model Aerosol Fields With Observations

[12] To constrain the aerosol fields used in the model, we use data from both the Moderate Resolution Imaging Spectroradiometer (MODIS), and from the Cloud Aerosol Lidar and Infrared Pathfinder Satellite Observation (CALIPSO). From MODIS we use clear-sky passive visible retrievals [*Remer et al.*, 2005] of aerosol optical depth (AOD) at a wavelength of 500 nm, and of the fine-mode aerosol fraction. These retrievals include improved estimates over land [*Levy et al.*, 2007], although there are still problems over bright surfaces. We use Collection 5 of the MOD04 aerosol product as included in the Level-3 MODIS Atmosphere Daily product gridded to 1 × 1°, and from this we create a July–October mean (2001–2008) clear-sky AOD climatology (Figure 2) for all aerosols and for the fine mode separately.

[13] In addition, we use active spaceborne lidar observations from CALIPSO to estimate the AOD at 532 nm of aerosol layers above clouds using the retrieval method by *Chand et al.* [2008]. We use two years of data (2006 and 2007) to create estimates of the mean AOD of elevated aerosol layers above low clouds, following the methodology described by *Chand et al.* [2009]. Figure 2 shows maps of mean total (fine + coarse) AOD at ~500 nm for all sky from CAM (PD simulation), for clear sky from MODIS, and for aerosol layers above clouds from CALIPSO. We additionally screen MODIS AOD for days where cloud fraction was less than 0.5 to reduce contamination from the effects of broken clouds [see, e.g., *Kaufman et al.*, 2005; *Loeb and Manalo-Smith*, 2005]. Good agreement of the spatial pattern of AOD is seen between the aerosol fields from the CAM and from the observations (Figure 2).

[14] We compare the fields using regression and mean values for the region with CALIPSO observations (7.5°N–22.5°S, 27.5°W–17.5°E). For the spatial correlation, $r = 0.87$ between CAM and MODIS total AOD and $r = 0.74$ between CAM and CALIPSO. The mean MODIS total AOD over ocean is 0.26 (versus 0.38 over land) while it is 0.24 (versus 0.40 over land) for CAM, indicating that our adjustment of the CAM fields produces a good match with the observations over both ocean and land. The CALIPSO AOD estimates are smaller (see Figure 2c), but this is expected since CALIPSO retrieval used here only captures those aerosol layers that lie above clouds, and the CAM aerosol fields indicate that there are carbonaceous aerosols both above and below clouds over the ocean. In addition, data from CALIPSO [*Chand et al.*, 2008] indicates that the aerosol layers above clouds have high Angstrom exponents of ~2, and so a fairer test of the fidelity with which biomass burning aerosol is represented in the model would be to compare CAM AOD from carbonaceous aerosols with MODIS fine mode AOD. These compare extremely well (Figures 2d and 2e and Figure 3), with mean values over ocean (land) of 0.16 (0.23) for MODIS fine-mode AOD and 0.14 (0.27) for CAM carbonaceous aerosols. Recalling the lower AOD for aerosols above clouds from CALIPSO (Figure 3, with means of 0.09 and 0.13 over ocean and land respectively), it is reasonable to conclude that perhaps 50–

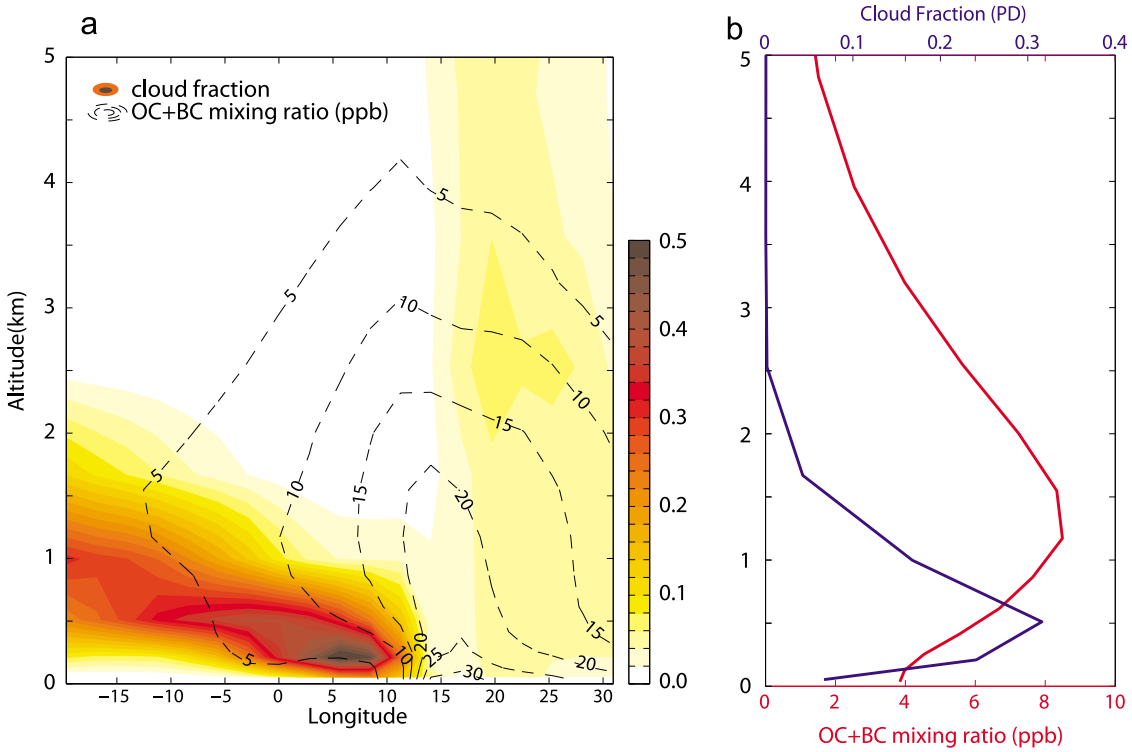

Figure 4. (a) Longitude-height cross section of July–October mean cloud fraction (colored contour) and mixing ratio of total carbonaceous aerosols (dashed line) from the CAM PD simulation, meridionally averaged over 0°–20°S. Note that the mean longitude of the southern African coastline is 12°E. (b) Vertical profiles of cloud fraction and mixing ratio of total carbonaceous aerosols averaged over ocean only from (0°–20°S, 20°W–30°E).

75% of the fine-mode AOD over the ocean in regions influenced by carbonaceous aerosols is coming from layers above clouds. The ratio of the mean AOD from CALIPSO to that from the MODIS fine mode is 0.56 over ocean (see also Figure 3). This is consistent with the model vertical aerosol structure: a longitude-height cross section of cloud occurrence and carbonaceous aerosols averaged over 0°–20°S from the CAM (Figure 4a) shows that the carbonaceous aerosols peak near the surface over land but the majority of the mass loading is above the low clouds in the marine boundary layer (MBL) over ocean (Figure 4b gives mean ocean profiles). This is also in agreement with in situ aircraft observations made over the ocean in this region [*Anderson et al.*, 1996] which show a peak in fine-mode aerosols at 3–4 km altitude and considerably lower aerosol concentrations close to the surface. This configuration of aerosols being primarily above the clouds over the ocean to the west of southern Africa is a result of prevailing winds in the MBL over the ocean mainly bringing relatively clean air from the south while the winds at 850 hPa and above are advecting aerosols from the South African continent [see also *Matichuk et al.*, 2007; *Chand et al.*, 2009].

2.2. Partitioning the Radiative Response Into Direct and Semidirect Components

[15] Differences between the PD and NC simulations are used to examine the effects of the biomass burning smoke on the radiative budget and regional climate. Here, we focus on the months of July to October, so all quantities we present are means over this period. We only consider shortwave effects here since the longwave effects of the changes in aerosols and the responses they incite in low clouds are small. Each of the simulations is run with an offline calculation of the aerosol direct radiative effect (DRE). Here we define DRE as that of the carbonaceous aerosols only since these are the only aerosols to change between the simulations. This allows us to parse the total change in net solar irradiance (at an arbitrary level and horizontal location) ΔF into four terms:

$$\Delta F = \{DRE_{CLR}(1-\overline{C})\} + \{\overline{C}\cdot DRE_{CLDY}\} + \{\overline{C}\cdot \Delta F_{CLDY,LWP}\} + \{\Delta C(\overline{F}_{CLDY} - \overline{F}_{CLR})\} \quad (1)$$

D1 D2 S1 S2

Throughout, the symbol Δ represents the difference between the two simulations (PD - NC), and F is the net solar irradi-

Table 1. Total Cloud Cover, Radiative Effects at the TOA, Surface, and Atmosphere, and Their Contributing Terms Averaged Over 20°W–50°E, 10°N–30°S, for the Land and Ocean Separately, and for Land and Ocean Together[a]

	Land			Ocean			Both Land and Ocean		
Variable	Mean	Median	σ*	Mean	Median	σ*	Mean	Median	σ*
$\overline{C}_{total}$	0.49	0.51	0.27	0.53	0.51	0.12	0.50	0.49	0.20
ΔC_{total}	0.003	0.004	0.015	0.020	0.017	0.025	0.011	0.009	0.023
					TOA (W m^{-2})				
Term D1	−0.8	−0.5	0.9	−1.4	−1.1	0.8	−1.2	−1.0	0.9
Term D2	1.0	0.8	0.9	2.3	1.0	3.5	1.6	0.9	2.5
Term S1	1.7	1.0	2.7	−0.7	−0.5	2.4	0.3	0.2	2.8
Term S2	−0.4	−0.3	1.2	−1.9	−1.5	2.5	−1.1	−0.7	2.0
Sum of all terms	1.5	1.3	2.8	−1.7	−1.6	2.8	−0.3	−0.4	3.2
					Surface				
Term D1	−9.3	−8.7	7.2	−4.5	−3.9	2.5	−6.6	−4.8	5.7
Term D2	−3.8	−2.7	3.5	−3.2	−2.4	2.6	−3.4	−2.4	3.1
Term S1	1.8	1.1	3.1	−0.9	−0.6	2.9	0.2	0.1	3.4
Term S2	−0.5	−0.3	1.3	−2.3	−1.7	2.9	−1.3	−0.8	2.4
Sum of all terms	−11.8	−11.9	7.7	−10.8	−9.3	7.7	−11.1	−10.2	7.6
					Atmosphere				
Term D1	8.5	7.3	7.0	3.1	2.8	1.8	5.5	3.5	5.4
Term D2	4.8	3.7	3.2	5.5	3.5	5.5	5.0	3.5	4.4
Term S1	0.0	0.0	0.4	0.2	0.1	0.4	0.1	0.1	0.4
Term S2	0.0	0.0	0.1	0.4	0.2	0.5	0.2	0.1	0.4
Sum of all terms	13.2	11.9	7.5	9.2	6.9	7.3	10.7	8.5	7.5

[a]The column σ* gives the standard deviation over space. An estimate of the uncertainty in the terms can be obtained from the difference between the sum of four terms and the model output total forcing ($\Delta F^{net}_{model} - \Delta F^{net}_{calculated}$). This error is less than 0.1 W m^{-2} for the TOA and surface effects, and slightly higher for the atmospheric effects. Contributing terms: D1, direct effect in clear sky; D2, direct effect in cloudy sky; S1, semidirect effect due to liquid water path changes; and S2, semidirect effect due to cloud cover changes.

ance. A derivation of (1) is given in Appendix A. The first term in equation (1), D1 $\{DRE_{CLR}\ (1 - \overline{C})\}$ is the aerosol direct radiative effect in clear-sky conditions weighted by the fractional clear-sky amount. The second term, in equation (1), D2 $\{\overline{C} \cdot DRE_{CLDY}\}$ is the aerosol direct radiative effect in cloudy-sky conditions weighted by cloud fractional amount. The sum of these two terms is the total aerosol direct radiative effect. The third term, S1 $\{\overline{C} \cdot \Delta F_{CLDY,LWP}\}$ is the semidirect aerosol effect in cloudy-sky conditions associated with changes in the cloud liquid water path (LWP). The fourth term, S2 $\{\Delta C\ (\overline{F}_{CLDY} - \overline{F}_{CLR})\}$ represents the semidirect aerosol effect due to cloud cover change. The semidirect aerosol effects in this study are a result of changes in the radiative heating profile and their effects on meteorological fields forced by presence of carbonaceous aerosols. Since we are using a slab ocean model, these meteorological changes include those stemming from surface temperature reductions due to reduced solar irradiance. Cloudy-sky solar flux is calculated from the model outputs using shortwave cloud radiative effect (SWCRE), i.e., $F_{\mathrm{CLDY}} = SWCRE/C + F_{CLR}$. The sum of the third and the fourth terms represents the total aerosol semidirect radiative effect. We calculate and examine these terms at the top of atmosphere and at the surface, and the difference between them constitutes the atmospheric aerosol radiative effect.

[16] We also define a radiative forcing efficiency by carbonaceous aerosols as the forcing ΔF (or term in (1) contributing to ΔF) per unit of carbonaceous aerosol optical depth (i.e., the difference in AOD between the PD and NC model runs), which has units of Wm$^{-2}\tau^{-1}$.

3. Results

3.1. Regional Maps of Aerosol Radiative Effects

[17] Table 1 and Figure 5 provide details of the time mean (July–October) shortwave radiative effects (flux differences) due to carbonaceous aerosols, averaged over the region for which the aerosol perturbations have been applied, i.e., 20°W–50°E, 10°N–30°S (see Figure 1). Table 1 gives mean, median and spatial standard deviation of the aerosol radiative effect and contributing terms (i.e., D1, D2, S1 and S2) at the TOA, the surface and for the atmosphere, broken down by ocean, land, and ocean + land respectively. Figure 5 presents maps of these terms including the sum total of all the effects.

3.2. Direct Radiative Effects and Efficiency

[18] Negative top of atmosphere clear-sky DRE (term D1) indicates that over dark surfaces aerosol scattering dominates (Figure 5a). Over the region of high surface albedo such as around the Kalahari Desert in southern Africa (Figure 5a), high surface albedo leads to weak positive clear-sky DRE at the TOA. Over the ocean, because there are extensive low clouds, the magnitude of term D2 (cloudy-sky DRE weighted by cloud cover) exceeds term D1 in the mean (Table 1). Term D2 is positive because the clouds are sufficiently bright, and the aerosol absorption sufficiently strong (Figures 3k and 3l), and agrees with observationally derived satellite estimates constrained with in situ aerosol single-scattering albedo [*Chand et al.*, 2009]. However, the cancellation between terms D1 and D2 in the mean over the ocean belies a highly spatially variable signal in cloudy-sky DRE (term D2, Figure 5b) compared with D1 (Table 1). Term D2 greatly exceeds D1 over the region where there is both extensive low cloud cover and carbonaceous aerosols (Figures 1 and 2 and Figure 10). In this region close to the southern African coast the carbonaceous aerosol layers are primarily located above low clouds (Figure 4) which maximizes the effects of aerosol absorption and leads to a strong positive DRE at the TOA.

[19] Over land, the TOA DRE terms are smaller than over ocean, but there is more or less complete cancellation of terms D1 and D2 leading to near-zero DRE. This is interesting given that the low cloud cover is much smaller over land than over ocean (Figure 6). However, there is considerable total cloud over the land (almost 50%, see Table 1), much of which is in the form of thin cirrus. *Satheesh* [2002] uses radiative transfer calculations to show significant positive DRE at the TOA even the case where clouds with an optical thickness of 4 are above absorbing aerosols. The TOA DRE would become more positive still for optically thinner clouds.

[20] The atmospheric aerosol radiative effect (i.e., the difference between TOA and surface) comes almost exclusively from the DRE (Table 1 and Figures 5k–5n), which is

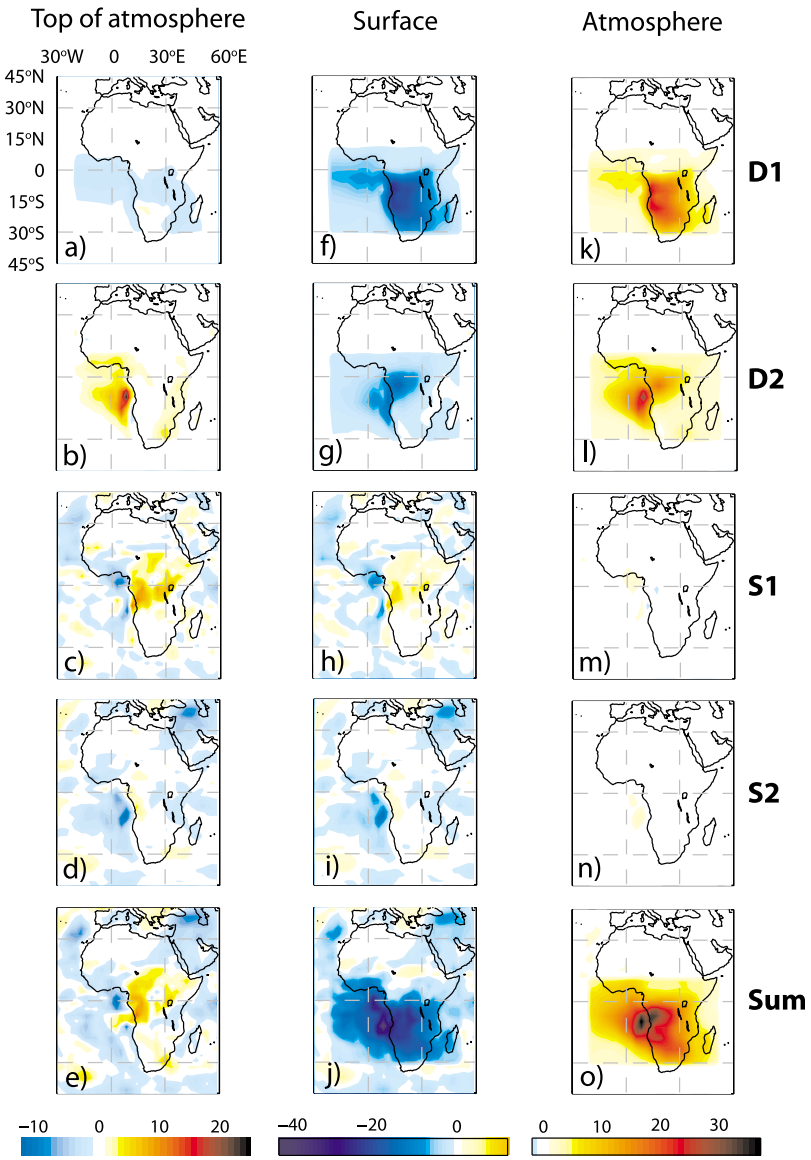

Figure 5. (a–e) Radiative forcing terms at TOA, (f–j) surface, and (k–0) atmosphere: Term D1 (Figures 5a, 5f, and 5k), Term D2 (Figures 5b, 5g, and 5l), Term S1 (Figures 5c, 5h, and 5m), Term S2 (Figures 5d, 5i, and 5n), and sum of the four terms (Figures 5e, 5j, and 5o). Note that the same color scale is used for each panel, but a different portion of that color scale appropriate for each column is shown.

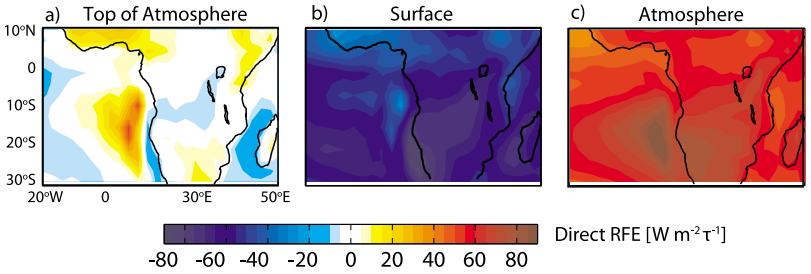

Figure 6. Total direct radiative forcing efficiency ($Wm^{-2}\tau^{-1}$) (a) at the top of atmosphere (TOA), (b) at the surface, and (c) for the atmosphere.

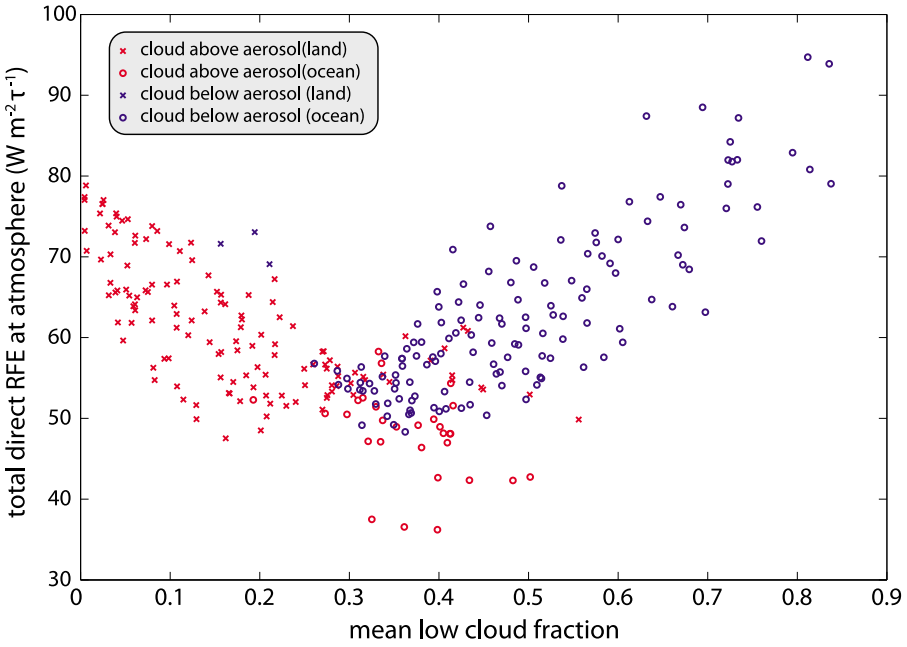

Figure 7. Mean low cloud fraction against total direct RFE at atmosphere, colored by whether cloud layer is above (red) or below (blue) the aerosol layer.

strongly positive due to aerosol absorption of solar radiation. The clear-sky, atmospheric DRE (not weighted by clear-sky amount) linearly increases with AOD (r = 0.97). The cloudy-sky atmospheric DRE has a maximum where low cloud fraction has its relative maximum (Figure 5l). This further emphasizes the importance of low clouds underlying the absorbing aerosol layers.

[21] The DRE at the surface is strongly negative (Table 1 and Figures 5f and 5g) and is dominated by the clear-sky contribution over the land. Over ocean, there are approximately equal contributions from the clear and cloudy sky, which is interesting and has potentially important implications for the impacts on the upper ocean heat budget, which can feed back and impact the semidirect effects.

[22] Because the aerosol DRE is approximately linearly dependent on aerosol optical depth [*Chýlek and Coakley*, 1974], the dependence of the DRE on other aerosol and cloud properties can be efficiently examined using the concept of radiative forcing efficiency (RFE, the radiative effect per unit of AOD change between the PD and NC simulations). Maps showing the total direct RFE (sum of terms D1 + D2 per unit of carbonaceous aerosol optical depth) for the TOA, surface, and the atmosphere are shown in Figure 6. Consistent with *Chand et al.* [2009], there is a high correlation between mean low cloud fraction and total direct RFE for both the atmosphere and TOA over ocean (r = 0.84 for RFE at the TOA and r = 0.79 for the atmospheric RFE). The correlation is weaker over land (r values of 0.73 and 0.66 for the TOA and atmosphere respectively), but is still strong, highlighting the important role that clouds play in determining the DRE of biomass burning aerosols. In contrast, the correlation of the direct RFE at the surface with low cloud cover is strong over land (r = 0.92) while no significant correlation is found over ocean (r = 0.17), a point to which we return below.

[23] For the atmospheric absorption, the two key factors that contribute to the land-ocean contrasts are the vertical profile of aerosols relative to cloud height and the albedo of the surface underlying the aerosol layer. Figure 7 shows a contrasting dependence of total atmospheric direct RFE as a function of mean low cloud fraction. When clouds are primarily found above aerosol layers, the total atmospheric absorption RFE weakens with cloud cover, whereas it strengthens when aerosol layers are primarily above clouds. Since aerosol layers are primarily found above clouds over ocean and in/below clouds over land (Figure 4), the atmospheric direct RFEs over ocean and land have opposing dependencies on low cloud cover. When the absorbing aerosols are in and below the low clouds, the aerosol absorption of solar radiation is weaker because clouds reflect a significant fraction of the incoming solar radiation before it can reach the aerosol layer. However, when the absorbing aerosols are above clouds, aerosol absorption is stronger with more low cloud cover because reflection from clouds gives the aerosols a second opportunity to absorb solar radiation.

[24] As mentioned above, the surface direct RFE is poorly correlated with low cloud cover over ocean (r = 0.17), but is well-correlated with cloud LWP (r = 0.79) indicating that thick low clouds shield the ocean surface from the radiative effects of aerosols since high LWP regions are those with the weakest negative surface RFE (Figure 6). Over land, the surface direct RFE is well correlated with low cloud cover and liquid water path, but since low cloud fraction and cloud liquid water path over land are tightly coupled (r = 0.85), it seems reasonable to suggest that it is the thickness of the cloud that is the primary control on the surface direct RFE over land as it is over ocean.

[25] Over land, clear-sky direct RFE at the TOA is highly dependent on surface albedo. Surface albedo explains almost 90% of the variance in clear-sky direct RFE at TOA

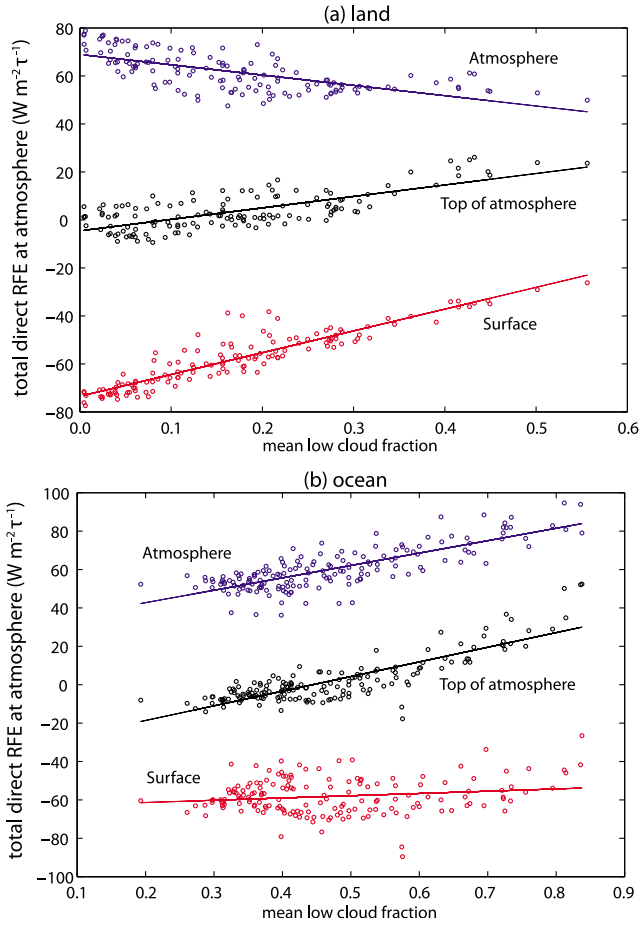

Figure 8. Surface, atmospheric, and TOA direct RFE from the model against the mean low cloud fraction over (a) land and (b) ocean. The critical low cloud fractions C^* where the sign of the TOA direct effect changes from negative to positive are ~0.10 (land) and 0.44 (ocean).

over land and the critical surface albedo where the direct RFE changes its sign is 0.23 ± 0.01. All-sky direct RFE at the TOA becomes less negative as low cloud cover increases over both land and ocean. Over land, where the aerosols are mainly in and below the low clouds, the positive atmospheric DRE weakens with increasing low cloud fraction at about half of the rate the negative surface DRE weakens. Therefore the all-sky RFE at the TOA, which is the sum of the surface and atmospheric RFE, increases with low cloud cover. The total direct RFE increases with low cloud cover over the ocean as well, but the mechanism is different than that over land. Since the albedo of sea surface is low, the aerosol reflection of solar radiation leads to negative RFE at the TOA where cloud cover is low. However, as the low cloud cover increases, absorption of solar radiation due to the aerosol layers above the clouds reduces the radiation going out at TOA and leads to positive RFE.

[26] Over the ocean, the linear slope of the all-sky direct RFE at the TOA against low cloud cover (Figure 8) is similar to that from observationally derived estimates by *Chand et al.* [2009]. *Chand et al.* [2009] used an observational data of aerosol optical depth for layers above clouds from CALIPSO, together with MODIS-derived cloud optical thickness, to run a radiative transfer model to estimate the mean direct radiative effect of elevated aerosol layers above regions with partial cloudiness. Most land regions were excluded from the Chand et al. analysis, so their results should be compared to our results over ocean. The TOA direct RFE over ocean increases from −33 to +43 W m^{-2} as low cloud fraction increases from zero to unity in the model (Figure 8), compared with −35 to +51 W m^{-2} from Chand et al., in good agreement. The TOA results, however, mask the fact that there are considerable differences in the surface and atmospheric direct RFE low cloud trends (Figure 8) which largely offset each other. Specifically, we find that the increase of the atmospheric direct RFE with cloud fraction in the model is approximately twice as large as that by *Chand et al.* [2009], while the model surface direct RFE increases much more weakly with cloud cover in the model compared with the observations. Overall, the model atmospheric direct RFE is lower than that found by *Chand et al.* [2009]. Some of this behavior may be explained by the fact that the Chand et al. study only considered aerosol optical depth above clouds while our simulations incorporate the effects of aerosols regardless of position in the vertical column. The observational methodology would therefore be expected to enhance the effects of clouds on the atmospheric absorption compared to cases where the aerosols are sometimes in or below clouds as they are in the model (and in reality). On the other hand, the largest discrepancies are found for low cloud fraction suggesting that the aerosol single scattering albedo is also responsible. We note that the single scattering albedo (SSA) in the model (see, e.g., Figure 9) is typically higher than the value of 0.85 assumed by *Chand et al.* [2009], which was set to be consistent with in situ and surface-based remote sensing over southern Africa [*Leahy et al.*, 2007]. However, we note that the mean aircraft-derived SSA values for aged elevated aerosol layers during the SAFARI 2000 field experiment was closer to 0.9 [e.g., *Haywood et al.*, 2003; *Keil and Haywood*, 2003; *Osborne et al.*, 2003]. Thus the spread of model SSA values seen in Figure 9 is in slightly better agreement with the aircraft data than with the ground-based studies over land. *Haywood et al.* [2003] found that the SSA of biomass burning aerosols increases as the aerosol ages, which can reconcile the differences between the land-closer-to-source land-based and aged plume aircraft studies, and explain why the model results agree better with the latter over the ocean. Another factor that might affect differences between the model and observationally derived RFEs is that the model SSA has spatial variability whereas *Chand et al.* [2009] assumed constant (SSA = 0.85). The discrepancies between the model and observationally derived direct RFEs may therefore not entirely be due to a poor model representation of the aerosol direct effects. *Chand et al.* [2009] found a dependence of the critical cloud fraction (C^*, the cloud fraction at which total direct RFE at the TOA changes its sign from negative to positive) on aerosol SSA. Since direct $RFE_{ALL\text{-}SKY} = (1 - C) \times RFE_{CLR} + C \times RFE_{CLDY}$, the critical cloud fraction C^* is derived by setting $RFE_{ALL\text{-}SKY} = 0$, to give

$$C^* = \left(\frac{RFE_{CLR}}{RFE_{CLDY}} + 1\right)^{-1} \quad (2)$$

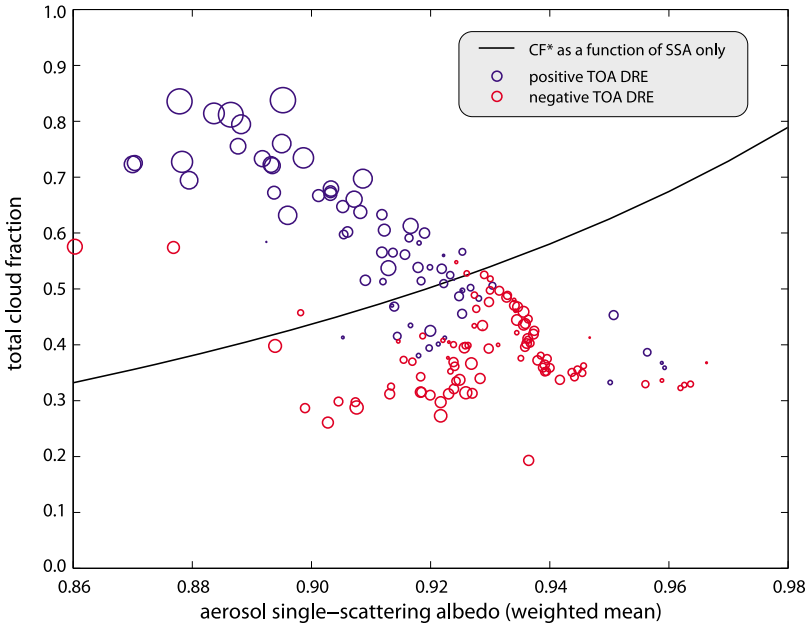

Figure 9. Total cloud fraction versus weighted mean aerosol SSA (SSA weighted by aerosol loading at each level) for model columns over ocean; black line shows the derived cloud critical fraction line; circles: positive (blue) and negative (red) total direct RFE at TOA; the size of circles indicates the magnitude of the forcing.

Over ocean where surface albedo is universally low, we use linear regression of the direct TOA RFE_{CLR} and RFE_{CLDY} against aerosol SSA from the model to give a curve of C^* against SSA. The aerosol SSA used here is the AOD-weighted mean from the PD and NC simulations. The correlation coefficients for TOA RFE_{CLR} and RFE_{CLDY} against the mean aerosol SSA are 0.74 and 0.16 respectively. Figure 9 shows that this derived function separates regions of positive and negative all-sky TOA direct RFE fairly well even though it contains a significant error range due to low correlation between cloudy-sky direct RFE and aerosol SSA. As the aerosols become more absorbing (lower SSA), the critical cloud fraction reduces from ~0.7 for SSA = 0.96 to ~0.33 for SSA = 0.86. Alternatively, from Figure 8 we can infer that C^* is ≈0.44 over ocean for the region as a whole. *Chand et al.* [2009] found that $C^* \approx 0.4$ for SSA = 0.85, which is a little higher than for the model simulations (at the same SSA), although the model SSA is in most places higher than that assumed in the observational analysis, which leads to a slightly higher C^* for the model as a whole. We think that this is because the model-derived SSA includes aerosol species other than carbonaceous aerosols which are likely to be less absorbing. Nevertheless, the dependence of C^* on the aerosol SSA is consistent with that found in the observational analysis (see auxiliary material for *Chand et al.* [2009]), and these findings give us some confidence that the configuration of aerosol and cloud fields in the model are a reasonably faithful representation of reality.

3.3. Semidirect Radiative Effects

[27] Table 1 shows that the semidirect radiative effects at the TOA have magnitudes comparable to the direct radiative effects, and therefore play an important role in determining the net forcing at TOA. However, there are important land-ocean contrasts in the semidirect effects. Cloud responses over the ocean (Table 1) are dominated by *increases* in cloud cover (with little LWP change overall), while land responses are dominated by *reductions* in LWP (with little cloud cover change). We will examine reasons for the cloud changes in the following sections. It is also important to note that the semidirect atmospheric radiative effect (Figures 5m and 5n) indicates that changes in cloud cover and LWP have only small effects on the shortwave absorption in the atmosphere compared with the absorption by aerosols themselves. Thus, the surface and TOA semidirect effects are almost equal (Table 1).

[28] The mean semidirect effect at the TOA is positive over the land (+1.3 W m^{-2} for LWP and cloud fraction effects combined; see Table 1) and negative over the ocean (−2.6 W m^{-2}). This is broadly consistent with the synthesis by *Koch and Del Genio* [2010]. Also, the strong land-ocean differential is consistent with a recent climate model study [*Allen and Sherwood*, 2010] but whereas we find significantly negative TOA semidirect effect over the ocean, *Allen and Sherwood* [2010] find almost zero oceanic semidirect effect for the globe as a whole. However, our analysis is focused on a limited region where over most of the oceanic regions the aerosols overlay clouds, and is likely not be representative of the global ocean. Large eddy simulations of the response of marine stratocumulus to elevated absorbing aerosol layers found increases in LWP [*Johnson et al.*, 2004] rather than cloud cover changes. However, since these simulations began with an overcast cloud, this precludes cloud cover changes. We do note that in the heart of the subtropical stratocumulus sheet, our simulations do show increases in LWP (Figure 10) but these are largely offset by decreases elsewhere. Large eddy simulations of the stratocumulus-to-cumulus transition regime [*Johnson*,

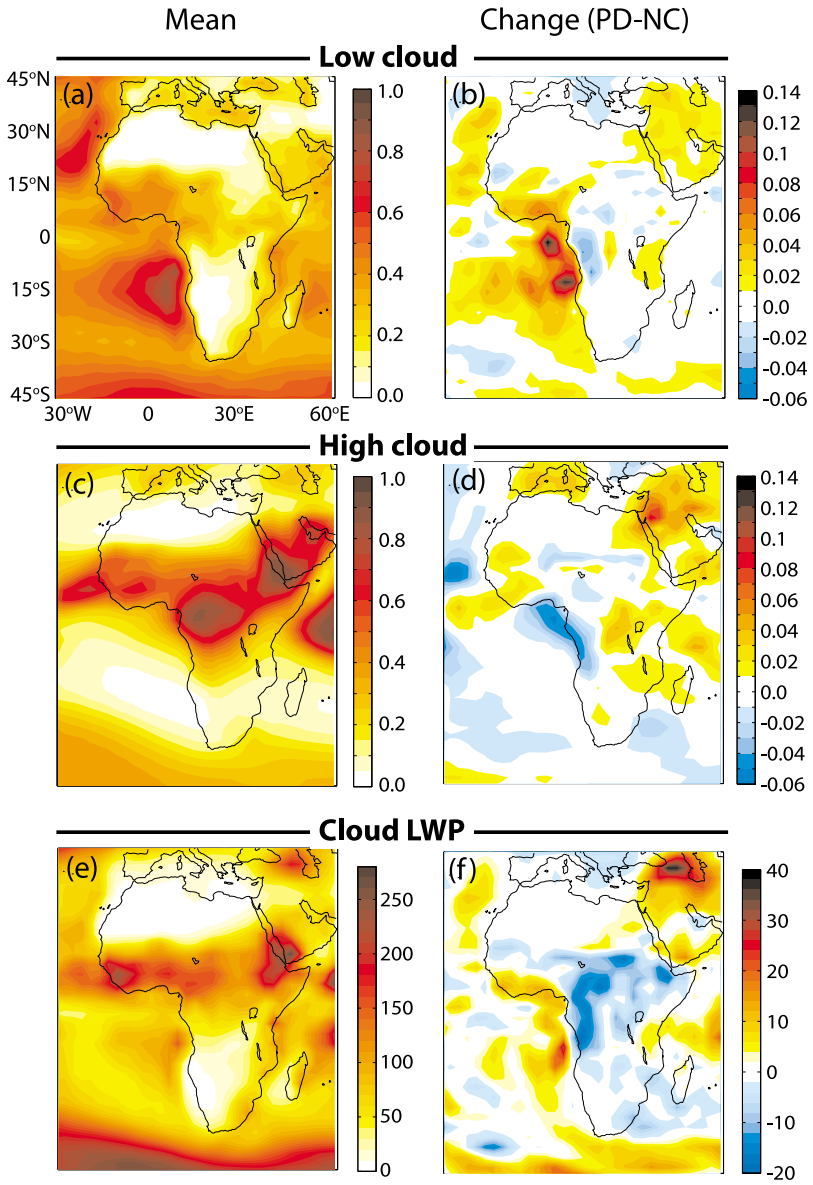

Figure 10. (a) Low cloud cover (clouds at and below 700 hPa) for the simulation with carbonaceous aerosols, (b) the change in low cloud cover between PD and NC simulations (with and without carbonaceous aerosols), (c) high cloud cover (clouds above 700 hPa) and (d) change in high cloud cover (PD-NC), (e) cloud liquid water path, and (f) change in liquid water path (PD-NC).

2005] did not consider the case of aerosols above clouds, but it is worth noting that most of the semidirect forcing in these simulations is attributable to cloud cover changes rather than cloud LWP changes.

[29] The spatial patterns of semidirect effects (Figures 5c and 5d) are generally more variable than those for the DRE indicating a complexity in the cloud responses in the model which includes nonlocal feedbacks. Over the ocean the TOA semidirect radiative effect due to cloud cover changes provides a significant offsetting of the cloudy-sky direct radiative effect (compare Figures 5b and 5d) and not surprisingly these effects maximize off the Angolan coast (5°S–15°S) where the carbonaceous AOD is maximal (see Figure 1) and the cloud cover is large (Figure 10). Over the land, the TOA semidirect effect adds to the positive cloudy-sky DRE, making the impact of clouds on the total radiative effect at the TOA significantly positive.

[30] Interestingly, the total TOA radiative effect (sum of terms D1, D2, S1, and S2) is almost equal and of opposite sign over the ocean and land. Since the land cover in our focus region is slightly less than 50%, this indicates that the total TOA radiative effect for the region as a whole is close to zero.

[31] The semidirect radiative forcing efficiency SRFE can be defined analogously to the direct RFE as the sum of terms S1 and S2 in equation (1) per unit of AOD change between the PD and NC simulations. As with the direct RFE we calculate the SRFE at the surface, for the atmosphere, and at the TOA. However, since we find that the atmospheric semidirect radiative forcing is very small, factors controlling

Table 2. Radiative Forcing and Cloud Fraction Comparison With (CONTROL) and Without (CLDMOD) the Klein and Hartmann Stability-Based Diagnostic Parameterization of Marine Stratus Clouds, 30°W–50°E, 10°N–30°S[a]

Variable	Over Land			Over Ocean		
	CONTROL	CLDMOD	r^2	CONTROL	CLDMOD	r^2
$\overline{C_{low}}$	0.17	0.18	1.00	0.47	0.37	0.73
ΔC_{low}	0.003	0.013	0.61	0.023	0.012	0.75
$\overline{C_{total}}$	0.49	0.49	1.00	0.53	0.44	0.70
ΔC_{total}	0.003	0.002	0.54	0.020	0.008	0.68
$\overline{CLDLWP}$	78.3	79.7	1.00	69.0	66.0	0.98
$\Delta CLDLWP$	−3.8	−1.4	0.71	2.7	1.3	0.69
$\overline{LTS}$	8.1	8.2	1.00	18.4	18.6	0.99
ΔLTS	0.50	0.54	0.78	0.47	0.44	0.99
ΔAOD	0.10	0.11	1.00	0.07	0.07	1.00
		Top of Atmosphere				
Term D1 (Wm^{-2})	−0.8	−0.8	1.00	−1.4	−1.7	0.92
Term D2 (Wm^{-2})	1.0	1.1	0.96	2.3	2.3	0.99
Term S1 (Wm^{-2})	1.7	1.0	0.70	−0.7	−0.4	0.65
Term S2 (Wm^{-2})	−0.4	−0.5	0.38	−1.9	−1.0	0.72
Sum of all terms (Wm^{-2})	1.5	0.7	0.68	−1.7	−0.8	0.60
Error (Wm^{-2})	0.03	0.08	0.37	0.005	0.003	0.84
		Surface				
Term D1 (Wm^{-2})	−9.3	−9.2	1.00	−4.5	−5.6	0.90
Term D2 (Wm^{-2})	−3.8	−3.9	1.00	−3.2	−2.2	0.84
Term S1 (Wm^{-2})	1.8	0.8	0.70	−0.9	−0.5	0.67
Term S2 (Wm^{-2})	−0.5	−0.6	0.36	−2.3	−1.2	0.74
Sum of all terms (Wm^{-2})	−11.8	−12.7	0.95	−10.8	−9.6	0.92
Error (Wm^{-2})	0.034	−0.030	0.18	−0.047	−0.038	0.77
		Atmosphere				
Term D1 (Wm^{-2})	8.5	8.3	1.00	3.1	4.0	0.90
Term D2 (Wm^{-2})	4.8	5.0	1.00	5.5	4.5	0.97
Term S1 (Wm^{-2})	−0.1	0.1	0.61	0.2	0.2	0.77
Term S2 (Wm^{-2})	0.0	0.1	0.20	0.4	0.2	0.81
Sum of all terms (Wm^{-2})	13.24	13.47	1.00	9.17	8.82	1.00
Error (Wm^{-2})	−0.011	0.10	0.51	0.05	0.04	0.77

[a]The column r^2 shows the spatial correlation between a particular variable for the CONTROL and CLDMOD simulations. Thus, a value $r^2 = 1$ indicates that the effect of changing the low cloud parameterization does not influence the spatial pattern of the variable. D1, direct effect in clear sky; D2, direct effect in cloudy sky; S1, semidirect effect due to liquid water path changes; and S2, semidirect effect due to cloud cover changes.

the TOA and the surface SRFE are essentially one and the same (compare Figures 5c and 5h and Figures 5d and 5i), which simplifies the analysis. We do not study the longwave component of the semidirect effects in this paper but note that because the model cloud changes are primarily associated with low clouds, we anticipate these effects to be quite small.

[32] The SRFE in general is related to changes both in cloud fraction and cloud LWP, as would be expected since we already saw above that significant semidirect effects are associated with changes in these parameters (Table 1 and Figure 5). Over the land, where the changes in cloud fraction ΔC between the PD and NC simulations are quite small (Table 1), the SRFE is well correlated with the change in LWP, with generally decreasing LWP leading to positive SRFE almost everywhere. The correlation coefficient between SRFE and ΔLWP is $r = -0.87$ over land. For both land and ocean taken together, we use multiple linear regression of SRFE against ΔC and ΔLWP which gives a multiple regression coefficient $r = 0.78$. However, we actually find that the semidirect radiative effect itself (rather than the efficiency) is better multiply correlated with ΔC and ΔLWP with a regression coefficient $r = 0.85$. This indicates that the changes in low clouds driven by the carbonaceous aerosols are not simply a function of the carbonaceous aerosol loading itself, but may be displaced in space most likely due to feedback processes that amplify the initial response. For example, whereas the heating of the troposphere due to the addition of absorbing aerosols would be expected to be more or less linearly related to the aerosol loading, the surface temperature response (itself a key determinant of the change in stability that might be expected to force cloud changes) will depend upon the surface direct RFE which is not simply a function of aerosol loading (see Figure 6a and associated discussion in section 3.2). We will examine further the causes of the cloud responses in section 3.4.

3.4. What Drives the Model Cloud Responses?

[33] The model cloud responses to carbonaceous aerosols that constitute the semidirect effects appear to be largely driven by increased lower tropospheric stability (LTS), which is typically defined as the difference in potential temperature between 700 hPa and the surface [see, e.g., *Klein and Hartmann*, 1993]. Increased LTS is caused both by increased atmospheric heating and surface cooling from the absorbing aerosols. There is a good physical basis for expecting that LTS increases over the ocean would drive increases in low cloud cover by increasing the inversion strength, suppressing cloud vertical extent and maintaining a

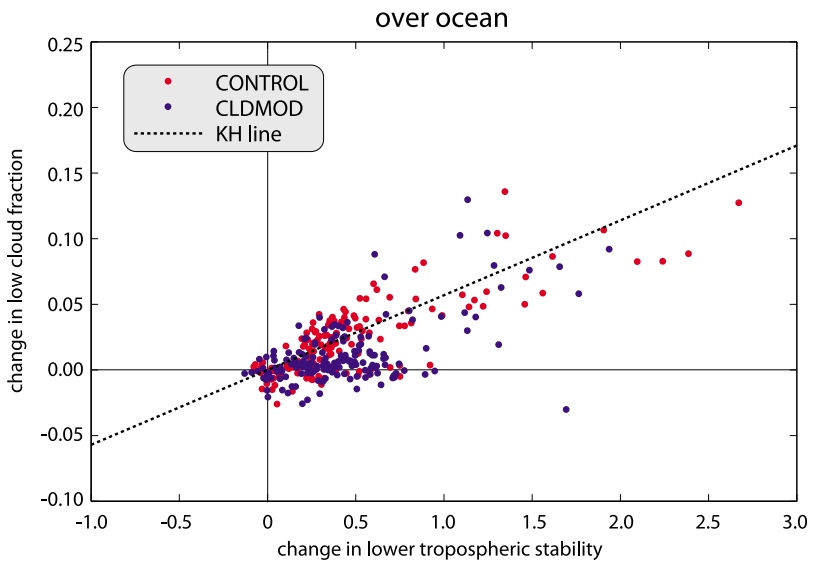

Figure 11. Changes (PD – NC) in low cloud fraction against changes in LTS over the ocean, for standard run (red) and CLDMOD (blue), and expected low cloud cover change from the Klein line (dashed black line).

well-mixed boundary layer [*Klein and Hartmann*, 1993; *Wood and Bretherton*, 2006]. Nevertheless, these previous studies are not focused on clouds driven by aerosol-driven stability changes, but by stability changes driven by continent-atmosphere dynamics [*Richter and Mechoso*, 2004, 2006; *Takahashi and Battisti*, 2007]. It is therefore useful to understand the extent to which the aerosol-driven cloud and stability changes resemble those driven by other processes.

3.4.1. Sensitivity to Model Cloud Scheme

[34] Three types of clouds are diagnosed by the cloud scheme in CAM3: marine stratus, convective, and layered clouds [*Boville et al.*, 2006]. The cloud scheme is described in some detail in the CAM3 documentation (available online at http://www.cesm.ucar.edu/models/atm-cam/). Marine stratus cloud fractional cover C_{stratus} is computed using, in part, the empirical linear relationship (the "Klein-line") between cloud amount C_{KH} and lower tropospheric stability (LTS) derived from observations by *Klein and Hartmann*, [1993]. Over land there is no marine stratus by definition, so $C_{\text{stratus}} = 0$. The diagnosed marine stratus cloud fraction is assigned to a layer below the layer of maximum static stability (inversion) and its amount is limited to be equal to the relative humidity RH_{max} within this layer, thus $C_{\text{stratus}} = \min(C_{\text{KH}}, RH_{\text{max}})$. The nonconvective cloud fraction C_{nonconv} for each grid box is the maximum of C_{stratus} and the layer cloud fraction C_{layer} derived from the relative humidity in the grid box, following *Slingo* [1987] and a height-dependent critical relative humidity [*Boville et al.*, 2006]. Thus $C_{\text{nonconv}} = \max(C_{\text{layer}}, C_{\text{stratus}})$. The total cloud fraction C for a given layer is the sum of convective cloud C_{conv} and C_{nonconv}, i.e., $C = \min(C_{\text{conv}} + C_{\text{nonconv}}, 1)$.

[35] In order to assess the impact of the stability-based parameterization on determining the low cloud fraction and the importance of changes in these clouds for the semidirect aerosol radiative effects, an additional set of PD/NC simulations was performed, but in this set the Klein-line is not used in the determination of low clouds. We refer to these additional simulations as cloud scheme modification CLDMOD. In CLDMOD, we set $C_{\text{stratus}} = 0$, so that $C_{\text{nonconv}} = C_{\text{layer}}$ and therefore $C = \min(C_{\text{conv}} + C_{\text{layer}}, 1)$. Thus, we neglect entirely the stratus cloud in the computation of total cloud fraction in order to see the importance of stratus cloud on the carbonaceous aerosol radiative forcing. Spatially, mean low cloud fraction in the PD or NC simulation with the cloud scheme modification CLDMOD is highly correlated ($r = 0.99$) with that in the CONTROL simulation over land, as expected since the model produces no stratus over land anyway. However, over ocean the low cloud fraction is everywhere decreased by neglecting stratus cloud (CLDMOD), indicating that stratus cloud fraction is generally greater than the layered cloud fraction produced from the *Slingo* [1987] parameterization in this region. However, the correlation of mean low cloud fraction between the CONTROL and CLDMOD modification remains quite high ($r^2 = 0.73$) demonstrating that even without the Klein and Hartmann diagnostic parameterization, the model is able to reproduce the geographical variability in mean low cloud cover over the ocean quite skillfully.

[36] Statistically significant differences are seen between CLDMOD and CONTROL in terms of the *change in low cloud fraction* due to carbonaceous aerosols (i.e., PD-NC). Even over land where the model produces almost no stability-based low cloud, the change in low cloud fraction due to the aerosols is different in both magnitude and spatial pattern. This indicates that changes in the atmospheric circulation associated with changes in the cloud scheme are important. That is, the effect of the cloud scheme changes are not solely local, but involve teleconnections associated with changing surface temperatures. This has been noted before in simulations of the tropical Pacific where adjustments to low clouds in the stratocumulus region over the cool part of the ocean effected changes throughout the rest of the basin [*Ma et al.*, 1996; *Gordon et al.*, 2000]. We do not explore this further in this manuscript.

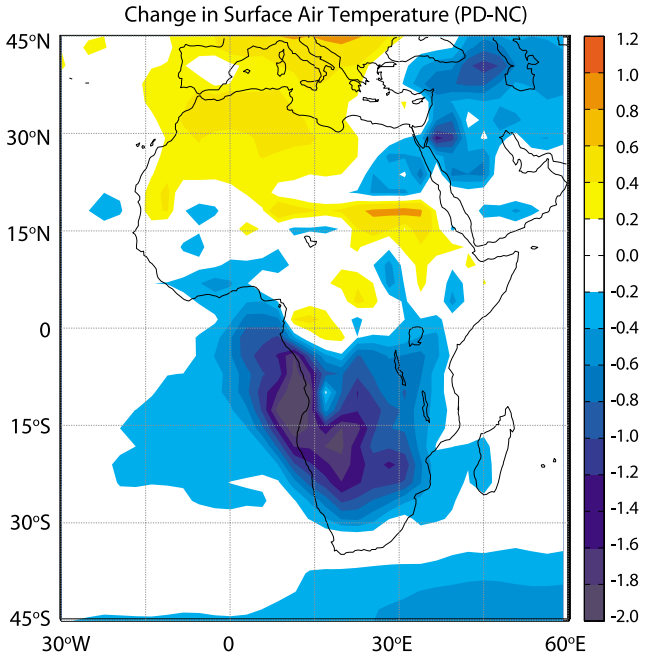

Figure 12. Change in surface air temperature between PD and NC runs. Strong cooling is observed throughout the region with strong negative radiative effect at the surface (see Figure 5j).

[37] Over ocean, the magnitude of the low cloud fraction changes due to carbonaceous aerosols are generally reduced over ocean when the KH parameterization is not used (see Table 2), but the sign of the changes remains the same. This is also the case for the changes in cloud LWP, and thus the semidirect effects are also reduced to around 60% of their values when the KH parameterization is included. Therefore, while the magnitude of the semidirect effect is uncertain, the sign is not simply a built-in response to free-tropospheric heating associated with the diagnostic KH parameterization. Although this does not assure that the modeled cloud cover responses over the ocean are consistent with the real-world responses, it does add credibility to the results suggesting oceanic increases in low clouds. Figure 11 shows the changes in low cloud fraction against those in LTS driven by carbonaceous aerosols for the KH and CLDMOD. As might be expected, the spatial correlation between changes in low cloud fraction and lower tropospheric stability over ocean is reduced (r^2 reduced from 0.64 with KH to 0.35 without it), but for most of the regions where the LTS increases most markedly, the low cloud cover also increases regardless of which parameterization is adopted. This gives us some confidence that the sign of the model cloud changes over ocean, both in terms of cloud fraction and cloud liquid water path, are robust with respect to changes in the way in which low clouds are parameterized. Since a large fraction of the total TOA aerosol radiative effect (sum of terms D1, D2, S1 and S2) is associated with the semidirect effects (Table 2) the total TOA radiative effect due to the carbonaceous aerosols is roughly halved by removing the KH parameterization. Thus, there remains considerable uncertainty regarding the magnitude of the aerosol effects associated with the parameterization of low clouds. The spatial pattern of the total aerosol effect at the TOA is altered but the effects with and without the KH parameterization are still quite well correlated over ocean and over land (Table 2). In contrast, at the surface and for the atmosphere the total radiative forcing is not largely effected by the stratus cloud parameterization since the majority of the total radiative forcing comes from direct forcing.

3.4.2. Lower Tropospheric Meteorological Changes Over Ocean

[38] Low cloud cover changes (PD – NC) over the ocean are significantly correlated with LTS changes (Figure 11), and these changes approximately follow those expected from the relationship by *Klein and Hartmann* [1993], with cloud cover increasing at approximately 0.05 per 1 K of ΔLTS.

[39] The low cloud cover increases from NC to PD over the ocean despite the specific humidity *decreasing* in the cloud layer. Unlike the situation described by *Perlwitz and Miller* [2010] where cloud cover increased due to increase in specific humidity exceeding the temperature warming, we find low cloud cover increases in our simulations are associated with a cooling of the marine boundary layer (Figure 12) which leads to saturation specific humidity decreases that are greater than the decrease in specific humidity, resulting in an increase in relative humidity (Figure 14). The surface temperature cools (Figure 12), and the surface latent heat flux reduces, because of the strong negative surface radiative effect (Table 1 and Figure 5), which is primarily a result of direct radiative effects (Table 1). However, although surface cooling is the primary driver of LTS increases, it is not the only driver, since the lower free troposphere warms (Figure 13a) by absorption of solar radiation by aerosols which reside primarily above cloud over the ocean (Figure 4).

[40] Another factor that might influence the marine low clouds is the significant change in large-scale vertical velocity caused by the aerosol absorption in the lower troposphere. Figure 13d shows that the carbonaceous aerosols reduce the subsidence by as much as 20–30% in the height range 0.5–4 km in the region of heaviest carbonaceous aerosol loading. In response, the model MBL deepens (Figures 13b and 13c indicate that the drop-off in relative humidity and the cloud fraction both move upwards). Over regions of the ocean not strongly impacted by biomass burning, deeper boundary layers tend to be accompanied by *decreased* cloud cover [e.g., *Wood and Hartmann*, 2006], and so it seems reasonable to suppose that, given this forcing alone, the cloud cover would decrease in response to the carbonaceous aerosol. The fact that this does not happen suggests that the effect of increased stability overwhelms that of reduced subsidence.

[41] Apart from changes in LTS and the large-scale vertical velocity over ocean, we might expect that reduced downwelling solar radiation at cloud top associated with absorption and scattering from the aerosols aloft might enhance the net (LW + SW) cloud top cooling which would drive thicker or more extensive clouds. We can crudely estimate the potential for this effect as being proportional to the diurnal reduction in low cloud fraction associated with the diurnal cycle of downwelling solar flux. Given this assumption, the expected low cloud cover increase due to the aerosol-induced reduction of cloud top downwelling solar flux reduction is only 0.0035, which less than one fifth of the actual modeled overall low cloud fraction increase (0.02) due

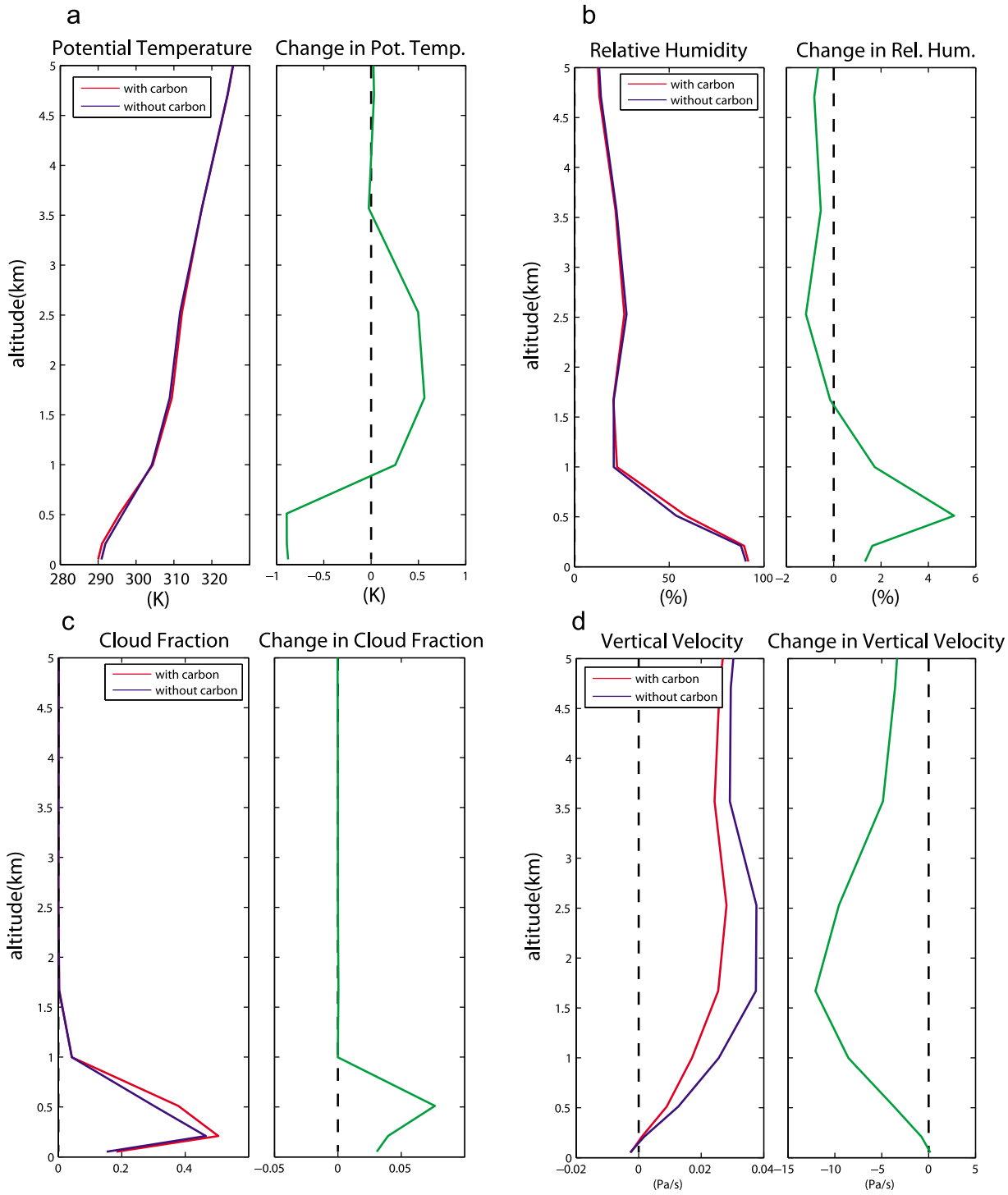

Figure 13. Means and changes (PD-NC) of (a) potential temperature, (b) relative humidity RH, (c) cloud fraction, and (d) vertical velocity, for a region (8°S–18°S, 0°–10°E) over the ocean with large cloud cover changes (see Figure 10).

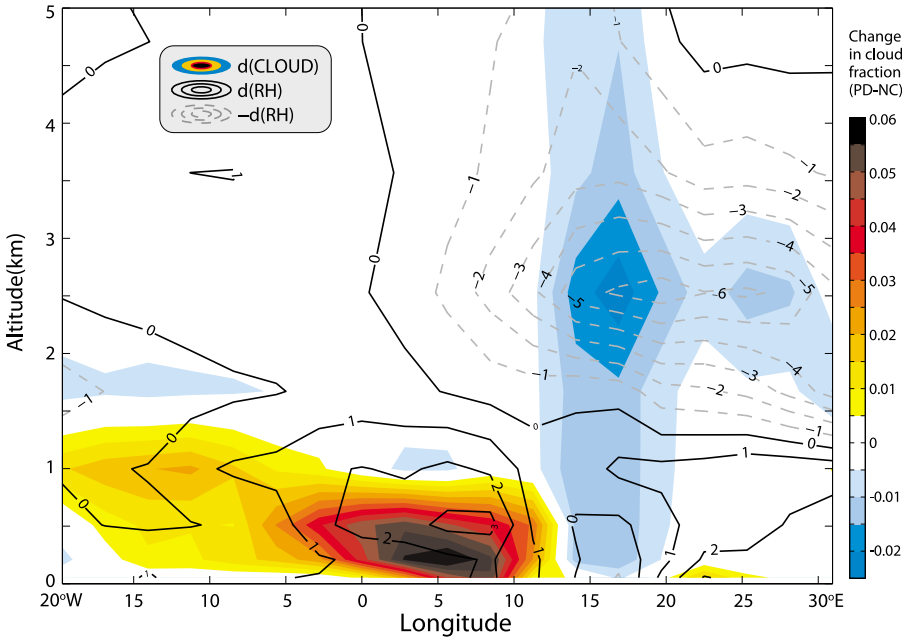

Figure 14. Meridional cross sections (averaged over 0°–20°S as in Figure 4) showing changes in low clouds (colored contours) and change in RH (solid lines show positive changes, and dashed lines show negative changes).

to the aerosol effects (see Table 1). Therefore, we conclude that the great majority of the low cloud cover increase is associated with factors other than reduced solar burn-off.

3.4.3. Lower Tropospheric Meteorological Changes Over Land

[42] Over the land, there are substantial reductions in cloud liquid water, but the low cloud cover changes are minimal (Figure 10). The low cloud cover is quite small over the land, since the clouds are predominantly cumuliform, but the clouds extend to higher levels in the vertical compared with the marine clouds. The increased stability is associated with low level cooling and warming aloft. This appears to reduce the vertical transport of moisture by suppression of shallow convection (Figure 14) resulting in a moister surface and a drier and warmer troposphere above this, especially between at altitudes 2–3 km where the aerosol heating is strongest. The reduction in shallow convection is the reason why the cloud liquid water path decreases over land. These results are in accordance with observational, cloud resolving and GCM modeling studies showing that absorbing aerosols tend to suppress cloud when the heating is within the cloud layer itself [*Ackerman et al.*, 2000; *Penner et al.*, 2003; *Johnson et al.*, 2004; *Feingold et al.*, 2005; *Johnson*, 2005; *Jiang and Feingold*, 2006; *Ming et al.* 2010].

3.5. Effects on Precipitation

[43] Figure 15 shows the mean precipitation rate during July–October together with the changes induced by the carbonaceous aerosols. The changes in precipitation rate are quite large in places, particularly around the NE part of the Gulf of Guinea and the adjacent land areas to the east. This area represents the southerly flank of the region of convective precipitation during the late boreal summer (Figure 15a) and is at the northerly limit of the strong aerosol-induced surface cooling (Figure 12). Thus, the strong surface cooling appears to be limiting the extent of the ITCZ during this season, and there is evidence that the Atlantic ITCZ is moved northward (Figure 15b). Weaker reductions in precipitation are also seen at the northern flank of the ITCZ too (Figure 15b). There are also increases in precipitation in the Arabian Peninsula (Figure 15b) but the model tends to produce way too much precipitation in this region compared with observations (Figure 15a) reflecting a long-term bias in CAM, and this signature should not be trusted.

4. Conclusion

[44] In this paper we use the CAM 3.0 model with a slab ocean to conduct simulations to explore the regional direct and semidirect effects of carbonaceous aerosols associated with biomass burning over southern Africa during the July–September dry season. In this region, burning over the southern African region generates large quantities of carbonaceous (both organic and black carbon) aerosols, which are lofted by convection to altitudes up to 5 km and then advected over the southeastern Atlantic Ocean where there are extensive low level clouds. We adjusted the model aerosols using satellite observations and introduced a new approach to quantifying the optical thickness of above-cloud aerosols. We neglected aerosol indirect effects in this particular study.

[45] Our primary findings are that the total TOA aerosol radiative effect of biomass burning aerosols over the southern African/Atlantic region is significantly altered by the inclusion of semidirect effects. These semidirect effects are primarily driven by changes in cloud cover and to a lesser extent liquid water path over the ocean, and by changes in liquid water path over land. The total TOA aerosol effect averaged over both land and ocean due to carbonaceous aerosols is quite close to zero since there is a significant

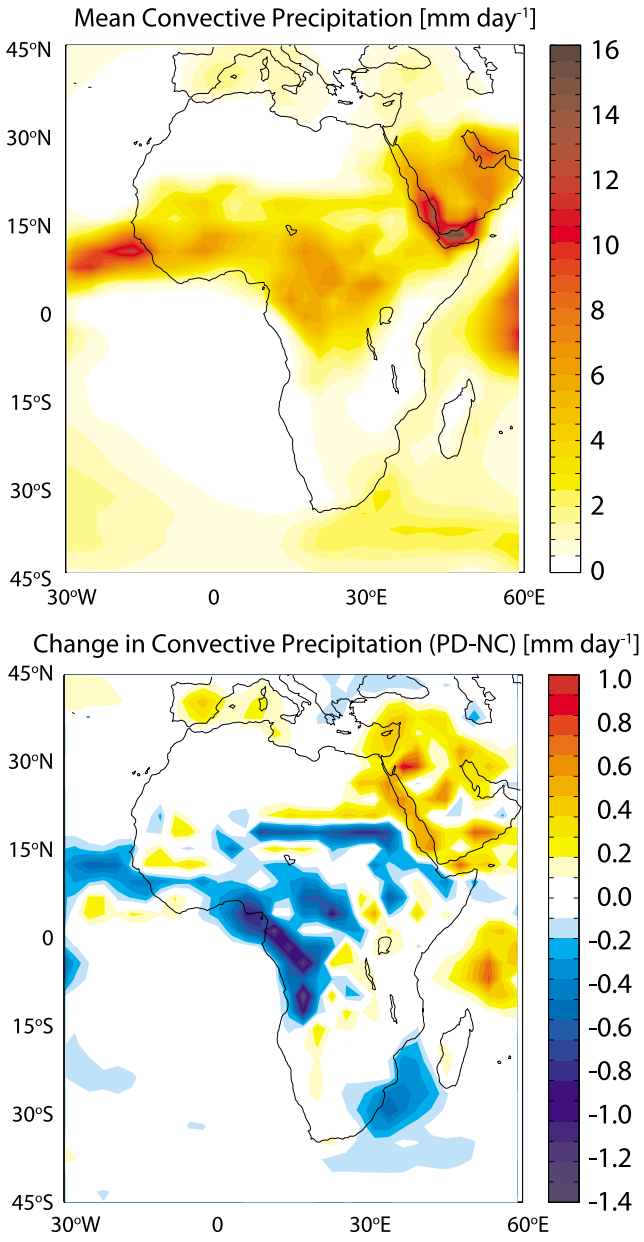

Figure 15. (a) Mean precipitation rate during July–October and (b) difference (PD-NC) in precipitation caused by carbonaceous aerosols.

degree of cancellation of direct effects by semidirect effects by land and ocean effects that are of opposite sign. The TOA direct effect over the ocean is strongly controlled by the mean low cloud cover in accordance with previous studies. In the model we find that the sign of the TOA direct effect changes sign from negative to positive at a cloud fraction of around 40–50% in accordance with previous observationally based estimates [*Chand et al.*, 2009], which suggests a good degree of skill in the model representation of the albedo of the clouds underlying the aerosol layers. Although the net forcing for the analyzed region at TOA is near zero, the differing signatures over land and ocean can produce significant changes in land/sea atmospheric circulations.

[46] The cloud changes responsible for the semidirect effects are driven by (1) reductions in near-surface temperature, (2) increases in free-tropospheric temperature, and (3) reduced large-scale subsidence, all three of which are driven to first order by the aerosol direct effects. The importance of surface cooling means that models not permitting a surface temperature response (e.g., atmosphere-only models) will most likely underestimate the semidirect effects. These effects increase marine low cloud cover and thickness and reduce convection and its associated liquid water over land. The results are sensitive to the parameterization of low clouds. Removing the Klein and Hartmann diagnostic parameterization from the cloud scheme does change the magnitude of the cloud responses but does not change their sign, which gives us some confidence that the general nature of the results presented here is robust. The mechanism of aerosol induced stability changes increasing cloud cover over ocean appears to explain the low cloud increases seen in GCM studies of elevated absorbing aerosol layers [*Penner et al.*, 2003; *Perlwitz and Miller*, 2010]. Although cloud cover changes dominate the ocean semidirect response as a whole over the ocean, near the maximum in low cloud cover we do see increases in LWP, which appears consistent with the observational findings in the region by *Wilcox* [2010]. This study does not consider cloud cover responses associated with elevated aerosol layers. In further work, the model could be used to determine if the thicker clouds associated with elevated pollution aerosols is partly driven by large-scale meteorological changes independent of the aerosols themselves.

[47] There also appear to be significant changes in the precipitation pattern driven by the carbonaceous aerosols. Overall, precipitation over the African convective region is decreased in our simulations, primarily through limitation of the extent of the convective region. Analyses suggest that much of the southern African biomass burning is anthropogenic and has therefore likely increased somewhat contemporaneously with increases in sulfate aerosols in the northern hemisphere [e.g., *Ito and Penner*, 2005]. One prevailing view is that reductions in Sahel precipitation over the second half of the 20th century may have been caused in part by increases in sulfate aerosol which cooled the northern Atlantic thus driving the ITCZ southward. Our results lead us to hypothesize that the increases in biomass burning aerosol may also play a significant role in limiting the horizontal extent of the ITCZ and driving down the magnitude of the convective precipitation in the northern African summer season. We plan to conduct further model studies to explore this issue in future work.

[48] Overall, the model results show the merits of conducting aerosol perturbation modeling studies focusing on limited areas to complement global aerosol-climate assessments and highly idealized process model studies.

Appendix A: Derivation of Equation (1)

[49] To derive equation (1) we begin by defining Δ as the difference of some field X between the present-day (PD) and no-carbon (NC) simulations:

$$\Delta X = X^{PD} - X^{NC}$$

where superscripts PD and NC indicate fields from PD and NC simulations respectively. Starting from the difference in

net all-sky shortwave radiative flux F_{all} (at any arbitrary level), we write:

$$\Delta F = F_{all}^{PD} - F_{all}^{NC} \tag{A1}$$

Now, we can break F_{all} down into clear and cloudy-sky components

$$F_{all} = C \cdot F_{CLDY} + (1 - C)F_{CLR} \tag{A2}$$

where C is cloud fraction, F_{CLDY} is cloudy-sky shortwave radiative flux, and F_{CLR} is clear-sky shortwave radiative flux. Substituting (A2) into (A1) yields

$$\begin{aligned}\Delta F = &\left[C^{PD} \cdot F_{CLDY}^{PD} + \left(1 - C^{PD}\right)F_{CLR}^{PD}\right] \\ &- \left[C^{NC} \cdot F_{CLDY}^{NC} + \left(1 - C^{NC}\right)F_{CLR}^{NC}\right]\end{aligned} \tag{A3}$$

The difference and the mean vertically integrated cloud fraction between the two simulations are defined as:

$$\Delta C = C^{PD} - C^{NC} \text{ and } \overline{C} = \frac{1}{2}\left(C^{PD} + C^{NC}\right)$$

The cloud fraction for each of the PD and NC simulations is then substituted into (A3) in terms of the difference and the mean cloud fraction (i.e., $C^{PD} = \overline{C} + \frac{1}{2}\Delta C$ and $C^{NC} = \overline{C} - \frac{1}{2}\Delta C$), which leads to

$$\begin{aligned}\Delta F = &\left(1 - \overline{C}\right)\Delta F_{CLR} \; + \; \overline{C} \cdot \Delta F_{CLDY} \\ &+ \; \frac{1}{2}\Delta C\left[\left(F_{CLDY}^{PD} \; + \; F_{CLDY}^{NC}\right) - \left(F_{CLR}^{PD} \; + \; F_{CLDY}^{NC}\right)\right]\end{aligned} \tag{A4}$$

We do the same with the clear-sky and cloudy-sky fluxes, by substituting them in into (A4) in terms of the average between the two simulations

$$2\overline{F}_{CLR} = \left(F_{CLR}^{PD} + F_{CLR}^{NC}\right), \;\; 2\overline{F}_{CLDY} = \left(F_{CLDY}^{PD} + F_{CLDY}^{NC}\right),$$

The change in cloudy-sky flux can be represented as the sum of the direct radiative effect of the aerosols and that associated with a change in liquid water path (LWP), i.e.

$$\Delta F_{CLDY} = \Delta F_{CLDY,Direct} + \Delta F_{CLDY,LWP}$$

which is also substituted into (A4) to yield equation (1) in the paper:

$$\begin{aligned}\Delta F = &\left\{DRE_{CLR}\left(1 - \overline{C}\right)\right\} \; + \; \left\{\overline{C} \cdot DRE_{CLDY}\right\} \\ &+ \; \left\{\overline{C} \cdot \Delta F_{CLDY,LWP}\right\} \; + \; \left\{\Delta C\left(\overline{F}_{CLDY} - \overline{F}_{CLR}\right)\right\}\end{aligned}$$

where $DRE_{CLR} = \Delta F_{CLR}$ and $DRE_{CLDY} = \Delta F_{CLDY,Direct}$.

[50] **Acknowledgments.** The authors would like to thank Duli Chand for helpful suggestions and discussion which improved the paper. This work was supported by the National Oceanographic and Atmospheric Administration grant NA070AR4310282. P.J.R. was supported by the Pacific Northwest National Laboratory under a Laboratory Directed Research and Development Project titled "Improving the Characterization of Aerosols as Forcing Agents in the Climate System."

References

Abel, S., E. J. Highwood, J. M. Haywood, and M. A. Stringer (2005), The direct radiative effect of biomass burning aerosols over southern Africa, *Atmos. Chem. Phys.*, *5*, 1999–2018, doi:10.5194/acp-5-1999-2005.

Ackerman, A. S., O. B. Toon, D. E. Stevens, A. J. Heymsfield, V. Ramanathan, and E. J. Welton (2000), Reduction of tropical cloudiness by soot, *Science*, *288*, 1042–1047, doi:10.1126/science.288.5468.1042.

Allen, R. J., and S. C. Sherwood (2010), Aerosol-cloud semi-direct effect and land-sea temperature contrast in a GCM, *Geophys. Res. Lett.*, *37*, L07702, doi:10.1029/2010GL042759.

Anderson, T. L., et al. (1996), Performance characteristics of a high-sensitivity, three-wavelength, total scatter/backscatter nephelometer, *J. Atmos. Oceanic Technol.*, *13*, 967–986, doi: 10.1175/1520-0426(1996)013<0967:PCOAHS>2.0.CO;2.

Boville, B. A., P. J. Rasch, J. J. Hack, and J. R. McCaa (2006), Representation of clouds and precipitation processes in the Community Atmosphere Model Version 3(CAM3), *J. Clim.*, *19*, 2184–2198, doi:10.1175/JCLI3749.1.

Chand, D., T. L. Anderson, R. Wood, R. J. Charlson, Y. Hu, Z. Liu, and M. Vaughan (2008), Quantifying above-cloud aerosol using spaceborne lidar for improved understanding of cloudy-sky direct climate forcing, *J. Geophys. Res.*, *113*, D13206, doi:10.1029/2007JD009433.

Chand, D., R. Wood, T. L. Anderson, S. K. Satheesh, and R. J. Charlson (2009), Satellite-derived direct radiative effect of aerosols dependent on cloud cover, *Nat. Geosci.*, *2*, 181–184, doi:10.1038/ngeo437.

Chen, W.-T., Y. H. Lee, P. J. Adams, A. Nenes, and J. H. Seinfeld (2010), Will black carbon mitigation dampen aerosol indirect forcing?, *Geophys. Res. Lett.*, *37*, L09801, doi:10.1029/2010GL042886.

Chýlek, P., and J. A. Coakley Jr. (1974), Aerosol and climate, *Science*, *183*, 75–77.

Collins, W. D., P. J. Rasch, B. E. Eaton, B. V. Khattatov, J.-F. Lamarque, and C. S. Zender (2001), Simulating aerosols using a chemical transport model with assimilation of satellite aerosol retrievals: Methodology for INDOEX, *J. Geophys. Res.*, *106*(D7), 7313–7336, doi:10.1029/2000JD900507.

Collins, W. D., et al. (2004), Description of the NCAR Community Atmospheric Model (CAM 3.0), *Rep. NCAR/TN-464+STR*, Natl. Cent. for Atmos. Res., Boulder, Colo.

Cook, J., and E. J. Highwood (2004), Climate response to tropospheric absorbing aerosols in an intermediate general-circulation model, *Q. J. R. Meteorol. Soc.*, *130*, 175–191, doi:10.1256/qj.03.64.

Cooke, W., B. Koffi, and J. M. Grégoire (1996), Seasonality of vegetation fires in Africa from remote sensing data and application to a global chemistry model, *J. Geophys. Res.*, *101*(D15), 21,051–21,065, doi:10.1029/96JD01835.

Costantino, L., and F.-M. Bréon (2010), Analysis of aerosol-cloud interaction from multi-sensor satellite observations, *Geophys. Res. Lett.*, *37*, L11801, doi:10.1029/2009GL041828.

Feingold, G., H. Jiang, and J. Y. Harrington (2005), On smoke suppression of clouds in Amazonia, *Geophys. Res. Lett.*, *32*, L02804, doi:10.1029/2004GL021369.

Gordon, C. T., A. Rosati, and R. Gudgel (2000), Tropical sensitivity of a coupled model to specified ISCCP low clouds, *J. Clim.*, *13*, 2239–2260, doi:10.1175/1520-0442(2000)013<2239:TSOACM>2.0.CO;2.

Hansen, J., M. Sato, and R. Ruedy (1997), Radiative forcing and climate response, *J. Geophys. Res.*, *102*(D6), 6831–6864, doi:10.1029/96JD03436.

Haywood, J. M., S. R. Osborne, P. N. Francis, A. Keil, P. Formenti, M. O. Andreae, and P. H. Kaye (2003), The mean physical and optical properties of regional haze dominated by biomass burning aerosol measured from the C-130 aircraft during SAFARI 2000, *J. Geophys. Res.*, *108*(D13), 8473, doi:10.1029/2002JD002226.

Ito, A., and J. E. Penner (2005), Historical emissions of carbonaceous aerosols from biomass and fossil fuel burning for the period 1870–2000, *Global Biogeochem. Cycles*, *19*, GB2028, doi:10.1029/2004GB002374.

Jiang, H., and G. Feingold (2006), Effect of aerosol on warm convective clouds: Aerosol-cloud-surface flux feedbacks in a new coupled large eddy model, *J. Geophys. Res.*, *111*, D01202, doi:10.1029/2005JD006138.

Johnson, B. T. (2005), Large-eddy simulations of the semidirect aerosol effect in shallow cumulus regimes, *J. Geophys. Res.*, *110*, D14206, doi:10.1029/2004JD005601.

Johnson, B. T., K. P. Shine, and P. M. Foster (2004), The semi-direct aerosol effect: Impact of absorbing aerosols on marine stratocumulus, *Q. J. R. Meteorol. Soc.*, *130*, 1407–1422, doi:10.1256/qj.03.61.

Kaufman, Y. J., et al. (2005), A critical examination of the residual cloud contamination and diurnal sampling effects on MODIS estimates of aerosol over ocean, *IEEE Trans. Geosci. Remote Sens.*, *43*(12), 2886–2897, doi:10.1109/TGRS.2005.858430.

Keil, A., and J. M. Haywood (2003), Solar radiative forcing by biomass burning aerosol particles during SAFARI 2000: A case study based on measured aerosol and cloud properties, *J. Geophys. Res.*, *108*(D13), 8467, doi:10.1029/2002JD002315.

Klein, S. A., and D. L. Hartmann (1993), The seasonal cycle of low stratiform clouds, *J. Clim.*, *6*, 1587–1606, doi:10.1175/1520-0442(1993)006<1587:TSCOLS>2.0.CO;2.

Koch, D., and A. D. Del Genio (2010), Black carbon semi-direct effects on cloud cover: Review and synthesis, *Atmos. Chem. Phys.*, *10*, 7685–7696, doi:10.5194/acp-10-7685-2010.

Lau, W. K., M. K. Kim, and K. M. Kim (2006), Asian summer monsoon anomalies induced by aerosol direct forcing: The role of the Tibetan Plateau, *Clim. Dyn.*, *26*, 855–864, doi:10.1007/s00382-006-0114-z.

Lau, W. K. M., M.-K. Kim, K.-M. Kim, and W.-S. Lee (2010), Enhanced surface warming and accelerated snow melt in the Himalayas and Tibetan Plateau induced by absorbing aerosols, *Environ. Res. Lett.*, *5*, 025204, doi:10.1088/1748-9326/5/2/025204.

Leahy, L. V., T. L. Anderson, T. F. Eck, and R. W. Bergstrom (2007), A synthesis of single scattering albedo of biomass burning aerosol over southern Africa during SAFARI 2000, *Geophys. Res. Lett.*, *34*, L12814, doi:10.1029/2007GL029697.

Levine, J. S., W. R. Coffer III, D. R. Cahoon Jr., and E. L. Winstead (1995), A driver for global change, *Environ. Sci. Technol.*, *29*(3), 120–125.

Levy, R. C., L. A. Remer, S. Mattoo, E. F. Vermote, and Y. J. Kaufman (2007), Second-generation operational algorithm: Retrieval of aerosol properties over land from inversion of Moderate Resolution Imaging Spectroradiometer spectral reflectance, *J. Geophys. Res.*, *112*, D13211, doi:10.1029/2006JD007811.

Loeb, N. G., and N. Manalo-Smith (2005), Top-of-atmosphere direct radiative effect of aerosols over global oceans from merged CERES and MODIS observations, *J. Clim.*, *18*, 3506–3526, doi:10.1175/JCLI3504.1.

Ma, C.-C., C. R. Mechoso, A. W. Robertson, and A. Arakawa (1996), Peruvian stratus clouds and the tropical Pacific circulation: A coupled ocean-atmosphere GCM study, *J. Clim.*, *9*, 1635–1645, doi:10.1175/1520-0442(1996)009<1635:PSCATT>2.0.CO;2.

Matichuk, R. I., P. R. Colarco, J. A. Smith, and O. B. Toon (2007), Modeling the transport and optical properties of smoke aerosols from African savanna fires during the Southern African Regional Science Initiative campaign (SAFARI 2000), *J. Geophys. Res.*, *112*, D08203, doi:10.1029/2006JD007528.

Ming, Y., V. Ramaswamy, and G. Persad (2010), Two opposing effects of absorbing aerosols on global-mean precipitation, *Geophys. Res. Lett.*, *37*, L13701, doi:10.1029/2010GL042895.

Morgan, M. G., P. J. Adams, and D. W. Keith (2006), Elicitation of expert judgments of aerosol forcing, *Clim. Change*, *75*, 195–214, doi:10.1007/s10584-005-9025-y.

Osborne, S. R., J. M. Haywood, P. N. Francis, and O. Dubovik (2003), Short-wave radiative effects of biomass burning aerosol during SAFARI2000, *Q. J. R. Meteorol. Soc.*, *130*, 1423–1447.

Penner, J. E., S. Y. Zhang, and C. C. Chuang (2003), Soot and smoke aerosol may not warm climate, *J. Geophys. Res.*, *108*(D21), 4657, doi:10.1029/2003JD003409.

Perlwitz, J., and R. L. Miller (2010), Cloud cover increase with increasing aerosol absorptivity: A counterexample to the conventional semidirect aerosol effect, *J. Geophys. Res.*, *115*, D08203, doi:10.1029/2009JD012637.

Ramanathan, V., and G. Carmichael (2008), Global and regional climate changes due to black carbon, *Nat. Geosci.*, *1*, 221–227, doi:10.1038/ngeo156.

Rasch, P. J., N. M. Mahowald, and B. E. Eaton (1997), Representations of transport, convection, and the hydrologic cycle in chemical transport models: Implications for the modeling of short-lived and soluble species, *J. Geophys. Res.*, *102*(D23), 28,127–28,138, doi:10.1029/97JD02087.

Rasch, P. J., W. D. Collins, and B. E. Eaton (2001), Understanding the Indian Ocean Experiment (INDOEX) aerosol distributions with an aerosol assimilation, *J. Geophys. Res.*, *106*(D7), 7337–7355, doi:10.1029/2000JD900508.

Remer, L. A., et al. (2005), The MODIS aerosol algorithm, products, and validation, *J. Atmos. Sci.*, *62*(4), 947–973, doi:10.1175/JAS3385.1.

Richter, I., and C. R. Mechoso (2004), Orographic influences on the annual cycle of Namibian stratocumulus clouds, *Geophys. Res. Lett.*, *31*, L24108, doi:10.1029/2004GL020814.

Richter, I., and C. R. Mechoso (2006), Orographic influences on subtropical stratocumulus, *J. Atmos. Sci.*, *63*(10), 2585–2601, doi:10.1175/JAS3756.1.

Satheesh, S. (2002), Aerosol radiative forcing over land: effect of surface and cloud reflection, *Ann. Geophys.*, *20*(12), 2105–2109, doi:10.5194/angeo-20-2105-2002.

Schulz, M., et al. (2006), Radiative forcing by aerosols as derived from the AeroCom present-day and pre-industrial simulations, *Atmos. Chem. Phys.*, *6*, 5225–5246, doi:10.5194/acp-6-5225-2006.

Slingo, J. M. (1987), The development and verification of a cloud prediction scheme for the ECMWF model, *Q. J. R. Meteorol. Soc.*, *113*, 899–927, doi:10.1256/smsqj.47708.

Sud, Y. C., E. Wilcox, W. K.-M. Lau, G. K. Walker, X.-H. Liu, A. Nenes, D. Lee, K.-M. Kim, Y. Zhou, and P. S. Bhattacherjee (2009), Sensitivity of boreal-summer circulation and precipitation to atmospheric aerosols in selected regions–Part 1: Africa and India, *Ann. Geophys.*, *27*, 3989–4007. doi:10.5194/angeo-27-3989-2009.

Takahashi, K., and D. S. Battisti (2007), Processes controlling the mean tropical Pacific precipitation pattern. Part I: The Andes and the eastern Pacific ITCZ, *J. Clim.*, *20*, 3434–3451, doi:10.1175/JCLI4198.1.

Wilcox, E. M. (2010), Stratocumulus cloud thickening beneath layers of absorbing smoke aerosol, *Atmos. Chem. Phys.*, *10*, 11,769–11,777, doi:10.5194/acp-10-11769-2010.

Wood, R., and C. S. Bretherton (2006), On the relationship between stratiform low cloud cover and lower-tropospheric stability, *J. Clim.*, *19*, 6425–6432, doi:10.1175/JCLI3988.1.

Wood, R., and D. L. Hartmann (2006), Spatial variability of liquid water path in marine low cloud: The importance of mesoscale cellular convection, *J. Clim.*, *19*, 1748–1764, doi:10.1175/JCLI3702.1.

Yoshimori, M., and A. J. Broccoli (2008), Equilibrium response of an atmosphere-mixed layer ocean model to different radiative forcing agents: Global and zonal mean response, *J. Clim.*, *21*, 4399–4423, doi:10.1175/2008JCLI2172.1.

P. J. Rasch, Pacific Northwest National Laboratory, 902 Battelle Blvd., PO Box 999, MSIN K9-34, Richland, WA 99352, USA.

N. Sakaeda and R. Wood, Department of Atmospheric Sciences, University of Washington, Box 351640, Seattle, WA 98195, USA. (robwood@atmos.washington.edu)